



**UNIVERSITÉ
DE GENÈVE**
FACULTÉ DES SCIENCES



Geodynamical regimes in Earth-like exoplanets: A parameter study for linking the internal structure with atmospheres

Master Thesis

Mariana Carolina Villamil Sastre
`mariana.villamil@etu.unige.ch`

Center for Life in Universe (CVU)
Department of Astronomy
Department of Earth Sciences
Université de Genève

Supervisors:

Prof. Emeline Bolmont

Prof. Luca Caricchi

Dr. Mathilde Kervazo

September 6, 2023

Acknowledgements

First, I would like to thank my advisors, Prof. Emeline Bolmont, Prof. Luca Caricchi, and Dr. Mathilde Kervazo, for their incredible guidance during the development of this thesis and for believing in my skills and passion for studying planets. You inspired me to keep following the academic life, and I'm super grateful for more advisors like you!

Second, I would like to thank my family on the other side of the ocean, for supporting me in every step I give in my career and for doing astronomical efforts for helping me to arrive here. I have missed you every day since the day I left. I can get out of Colombia, but Colombia will never get out of me.

Third, I would like to thank the Network of Colombian Astronomy Students (RECA), for supporting me during these two years of the mentorship program, without your help nothing of this could be possible. Let's keep building a new country with a promising and peaceful future.

Also, thanks to all my old and new friends, who made these two years an incredible experience. For sharing their diverse cultures and beliefs with me, and making me feel a bit at home. Thanks to all of you.

Finally, we thank the Computational Infrastructure for Geodynamics (geodynamics.org) which is funded by the National Science Foundation under award EAR-0949446 and EAR-1550901 for supporting the development of ASPECT.

Abstract

Solid-state convection of rocky planetary mantles is essential to a planet's habitability over geological timescales. The starting point of main events, such as plate tectonics, is mainly controlled by this heat transfer efficiency. To understand better how this particular tectonic regime came about in Earth's evolution, and how this can be extrapolated to our understanding of the dynamical regime of Earth-like exoplanets and especially their outgassing, it is necessary to investigate under which conditions Earth-sized planetary mantles can produce enough melt that might deliver volatiles to the surface. In this study, I model the internal structure of Earth-sized exoplanets that serve as a basis for 2D heat transfer numerical simulations to explore the parameter space of different silicate mantle sizes and dynamical regimes. In this way, I investigated the optimal candidates for internal structure configurations and compositions, to break the primitive basaltic crust considering different heat sources. I applied my model to the particular case of the TRAPPIST-1 planets to constrain tidal dissipation that can be produced within their mantle according to different core sizes. I showed that Earth-like exoplanets with big cores are the best candidates to produce melt efficiently and consequently deliver more water content to the atmosphere.

Contents

Acknowledgements	i
Abstract	ii
1 Introduction	1
2 Theory	3
2.1 Characterization of rocky exoplanets	3
2.1.1 Constraining the internal structure from observations . . .	4
2.1.2 Trappist-1 system	6
2.2 Modeling of mantle’s dynamics	7
2.2.1 Reference internal structure model: PREM model of the Earth	7
2.2.2 Governing equations for mantle convection	8
2.2.3 Heating sources and partial melting	13
2.2.4 Planetary geodynamic regimes	16
3 Methodology	19
3.1 Computation of the internal structure	19
3.1.1 Silicate mantle composition	19
3.1.2 1D-references profiles computation for Earth-like planets .	20
3.1.3 Trappist-1 planets modeling	22
3.2 2-D mantle convection simulation using ASPECT	22
3.2.1 General set up and initial conditions for geodynamical sim- ulations	22
3.2.2 Thermal-lid thickness	25
3.2.3 Melting values computation	26

CONTENTS	iv
4 Results	28
4.1 Temperature profiles	28
4.1.1 Onset of convection	30
4.1.2 Melting production and water availability	32
4.1.3 Mobility regime	33
4.1.4 Impact of Heat sources	34
4.2 Internal structure of Trappist-1 planets	35
5 Discussion	37
6 Conclusions	40
A Appendix	A-1

Introduction

Since the first exoplanet around a sun-like star was found 28 years ago ([Mayor and Queloz, 1995](#)), several efforts from the astronomical community have been directed to improve the detection precision of these extrasolar planetary bodies. Many ground and space-based missions designed solely for the search of other siblings of the Solar System allow for a current record of more than 5438 exoplanets confirmed ¹. With such a number, the exoplanet community started to characterize the different populations found to answer questions such as: **How unique is our planet?**. Initially, many planets have been observed with a mass and radius consistent with a rocky composition (e.g. [Sotin et al. \(2007\)](#), [Dorn et al. \(2015\)](#)). Nevertheless, understanding the internal structure and composition of exoplanets based on their mass and radius can lead to several degeneracies ([Otegi et al., 2020a](#)). For this reason, the interest in determining the factors that optimize the life potential of an exoplanet ([Lenardic, 2018](#)) is a growing field of study.

So far, our planet is the only place we know that can sustain life as we know it. On Earth, we know that several factors as volcanic activity induced by plate tectonics, were crucial in our planet’s geological history ([Turcotte and Schubert, 2002](#)). In this way, the chemical feedback between the silicate mantle and the gaseous envelope around the Earth allowed the best conditions for life to evolve. Furthermore, the presence of water at the surface played a fundamental role in the habitability of the Earth, which in principle, is a condition given by factors such as the distance between the host star and the planet, which we know as ‘**The habitable zone**’ (HZ) ([Kasting et al., 1993](#)).

Observational methods dedicated to rocky exoplanet observations emphasize atmospheric characterization. However, these observations strongly relate to the planet’s interior dynamics, especially its outgassing history. For this reason, the exoplanet community is very interested in understanding the atmospheres of these planets, looking forward to finding any life-associated compounds lying in the atmosphere, better known as -biosignatures-. Many exoplanets with similar mass and radius as the Earth have been found orbiting their stars within this

¹[NASA Exoplanet Archive \(Updated on 05/23/2023\)](#)

distance range. For example, the multi-planetary system Trappist-1 (Gillon et al., 2017) consists of an M-dwarf type of star surrounded by a minimum of seven Earth-like planets, with at least three located in the HZ.

On Earth, plate tectonics is a key factor for life (e.g. Ward and Brownlee (2003), Maruyama et al. (2013)). This is due to the long-term carbon cycle, that lets carbonate rocks subduct into the deep mantle through the plate boundaries. Thanks to subduction, volcanism will outgas volatiles in the melted rocks to the surface, replenishing the atmosphere of CO₂ among other elements, strongly influencing a planet's climate evolution. At the same time, thanks to the subduction and convection, diverse and extensive topography was developed at the plate boundaries, playing an important role in other chemical cycles as the water cycle and geomorphological features that helped life to develop in the last 3.5Gy (Ballmer and Noack, 2021).

The occurrence of plate tectonics is directly linked to the thermal evolution of the planet. Although, the degeneracies around these exoplanets' observed mass and radius diversify the possible outputs on internal structure and composition (Otegi et al., 2020b). Therefore, determining the interior structure of a planet and simulating its interior dynamics contributes to the global understanding of how a planet evolves, including its long-term habitability (e.g. Frank et al. (2014); Driscoll and Bercovici (2013); Foley and Driscoll (2016); Stracke et al. (2016)). This thesis studied which internal structure and composition configurations are optimal for mobile lid regimes as a function of mantle convection vigor and a primary water budget at the upper mantle. For this purpose, this work explores all the parameter space of possible internal structures of rocky planets with an iron core, through 1-D models and, consequently, explores the heat transfer regime with 2D numerical simulations of convection in their rocky mantles.

In the first chapter, I will present the theory and characterization of the internal structure of exoplanets as well as the governing equations for mantle convection and resulting interior dynamical regimes. This will be followed by describing the exoplanetary system of interest: **Trappist-1**. The second chapter will outline the applied methods to simulate similar Earth's interior dynamics onto the parameter space we are exploring, and the assumptions made for rocky-cored exoplanets. Finally, the last three chapters will describe the details of the results obtained during the study and discuss how we interpret them to bring us to conclusions.

Theory

2.1 Characterization of rocky exoplanets

During the last years of exoplanet research, several detection methods have been used to characterize the large amounts of confirmed exoplanets. Radial velocities and transit methods are the methods that release the major amount of detections with missions such as Kepler (e.g. [Jenkins et al. \(2010\)](#); [Koch et al. \(2010\)](#)) and the follow-up studies with ground-based telescopes. These two main detection methods allow for assessing the mass (radial velocities) and radius (transit). A combination of both measurements is thus precious to infer the density, from which it is possible to have insight into the internal structure of planets. The detected exoplanets are typically plotted on top of a theoretical mass-radius relation to investigate the demographics of the different exoplanet populations. From these, it is possible to estimate the density corresponding to every planet and make some inferences about the bulk composition, internal structure, and constraints in the planet formation perspective (e.g. [Dorn et al. \(2017\)](#); [Valencia et al. \(2007\)](#); [Sotin et al. \(2007\)](#); [Seager et al. \(2007\)](#)).

In [Otegi et al. \(2020a\)](#), a revisited catalog of exoplanets was made based on how robust and reliable the measurements of mass and radius were, considering only small uncertainties (below 25%) for planets with masses below $120M_{\oplus}$. On this filtered sample of exoplanets, there was a clear distinction between two kinds of populations: the ones following the Earth-like composition (this means the relative composition of Fe, Si, and small amounts of H_2O , therefore assuming the rocky nature of these bodies), and those exoplanets following the volatile-rich composition (Figure 2.1).

The rocky exoplanet population shows planets with masses up to $25M_{\oplus}$, indicating the maximum core mass that can be produced at these specific density conditions. Conversely, the volatile-rich population shows a lower density and higher dispersion, indicating a possible gas accretion. Both populations are divided by the composition line of pure water ([Dorn et al., 2015](#)). Due to observational restrictions, the demographics of exoplanets are biased. This means

that the most massive planets are the easiest to detect. This way, the occurrence rate is expected to rise for lower planet masses as the detection bias decreases.

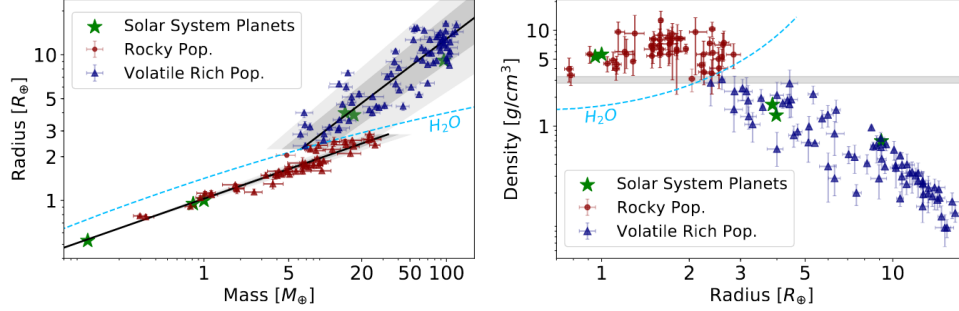


Figure 2.1: Mass-radius and density-radius relations from the revisited catalog described by [Otegi et al. \(2020a\)](#) showing the two main exoplanet populations below $120M_{\oplus}$. Rocky and volatile-rich populations are distinguished by the composition line of pure water and a density cut-off indicated by the gray region in both plots.

2.1.1 Constraining the internal structure from observations

Now that we have reviewed the characterization of rocky exoplanets and the revisited values of mass, radius, and inferred density, we can discuss the inferences about the internal structure from observations. We saw that for exoplanet interior characterization, the common practice is using mass-radius- plots where the mass and radius of exoplanets are compared to synthetically computed interior models.

Most studies concerned with rocky exoplanets (e.g. [Valencia et al. \(2007\)](#); [Sotin et al. \(2007\)](#); [Seager et al. \(2007\)](#); [Mocquet et al. \(2014\)](#)) have generally concentrated on computing mass-radius relations based on terrestrial-type interior structures and compositions. These studies show that different interior models can explain the observations within their uncertainties. However, such “forward” approaches do not quantify the inherent degeneracy of interior structure models. Indeed, for a given mass and radius, many internal structure configurations can lead to the same results (e.g. [Rogers and Seager \(2010\)](#); [Howe et al. \(2014\)](#)). This degeneracy is due to the many free parameters used when modeling the internal structure of exoplanets and the reduced observational constraints. To reduce this degeneracy, several models (e.g., [Grasset et al. \(2009\)](#); [Dorn et al. \(2015\)](#)) propose an inverse analysis to provide full probability distribution for the mantle and core composition and are based on the assumptions that elements that element abundances on a planet must follow the abundances trend in their host star.

In the same way, [Otegi et al. \(2020b\)](#) explores under what conditions observational constraints can improve interior estimates of planetary bulk abundances

taken from stellar proxies. Using the internal structure models of [Dorn et al. \(2017\)](#), an statistical analysis is performed to find which populations were the most degenerate when reproducing a sample of synthetic exoplanets representing the revisited catalog mentioned in the previous section. [Otegi et al. \(2020b\)](#) shows how depending on the M-R relation used, the internal structure configuration using different masses can vary significantly according to the measured radius. When examining planetary radii around 1.5 times that of Earth, the choice of the M-R relationship noticeably affects the estimation of the core mass (Figure 2.2). Likewise, this choice significantly impacts the inferred atmospheric mass for radii surpassing three Earth’s radii. For planets with radii near 2.5 times that of Earth, even slight differences in mass yield similar conclusions about their internal structures. However, due to the broad range of possible masses, relying solely on radius alone does not enable us to determine the internal structure confidently.

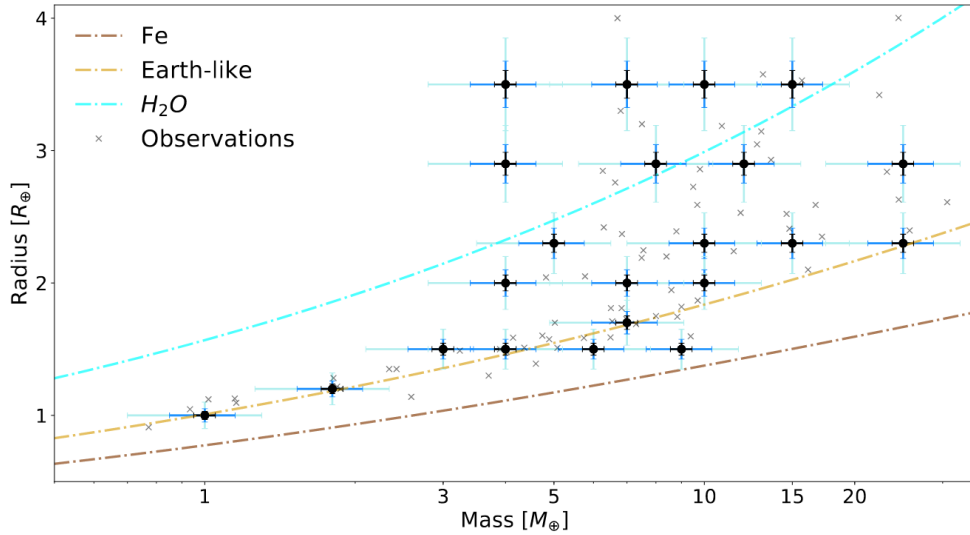


Figure 2.2: M-R relation for synthetic exoplanets that maps the revisited catalog described by [Otegi et al. \(2020b\)](#) for planets below $120M_{\oplus}$. The error bars represent the input uncertainties on the mass and radius of these synthetic populations.

Concluding that reducing the error bars on the observed mass and radius for planets below the Earth-like composition line leads to a more accurate determination of the core mass. In the same way, planets above the pure-water line lead to a more accurate determination of the atmospheric mass. Moreover, **planets between Earth-like and pure-water compositions are the most degenerate.**

2.1.2 Trappist-1 system

Among the detected planetary system with Earth-sized planets, the TRAPPIST-1 system is the most remarkable for its seven planets are similar in size, mass, density, and stellar heating to the analogs rocky planets Venus, Earth, and Mars in the Solar System. Trappist-1 planets are orbiting a low-mass star, forty light-years away (Gillon et al., 2017). Nevertheless, several observations show that at least three of these planets are located within the habitable zone, and are categorized as potential candidates for life-friendly conditions. The semi-major axes of these planets are between 1 to 6% of an AU, forming a compact system in resonance (Luger et al., 2017).

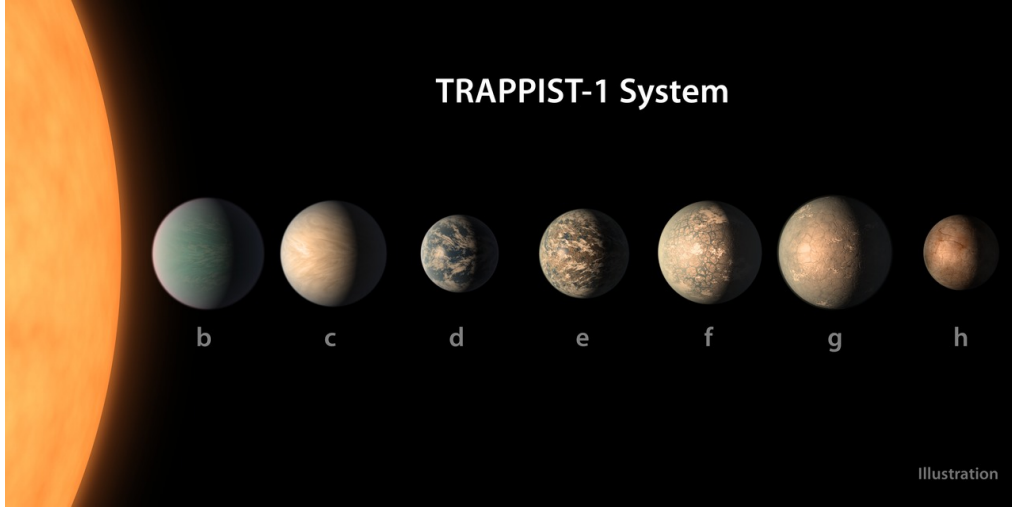


Figure 2.3: Artistic illustration of the TRAPPIST-1 system. Credit: NASA/JPL-Caltech

Thanks to observational techniques such as photometric transits, it was possible to retrieve precise measurements of each planetary radius (Ducrot et al., 2018). Furthermore, the large gravitational impact generated by the interaction between these planets has improved the density estimates on these planets. This has been described by Grimm et al. (2018) & Agol et al. (2021), indicating that the Trappist-1 planets have a rocky composition rich in volatiles.

Tidal dissipation plays a vital role in the energy budget of the TRAPPIST-1 planets. Tidal heat fluxes within this system are estimated to be at least ten times greater than the mean heat flux of Earth, as studied by Turbet et al. (2018) and Bolmont et al. (2020). In this way, the concept of a magma ocean on the closest planets is a plausible scenario as discussed by Barr et al. (2018) and Dobos et al. (2019). In the framework of this thesis, we computed the internal structure of the TRAPPIST-1 planets to investigate their tidal response.

2.2 Modeling of mantle's dynamics

2.2.1 Reference internal structure model: PREM model of the Earth

The Earth is the planetary body that we know the most. The main divisions on the internal structure of the Earth are the metallic and silicate portions, which at the same time are sub-divided into regions based on the propagation velocity of seismic waves (McDonough and Sun, 1995). The silicate shell surrounding the core comprehends the crust, the upper mantle, the transition zone, and the lower mantle. This was characterized by seismic discontinuities in the 1960s Earth's geophysical exploration. The most used 1-D model of Earth's internal structure has been the Preliminary Reference Earth Model (PREM) described by Dziewonski and Anderson (1981). In addition to mapping the P and S velocities, this model describes the density and attenuation as a function of depth (Figure 2.4)

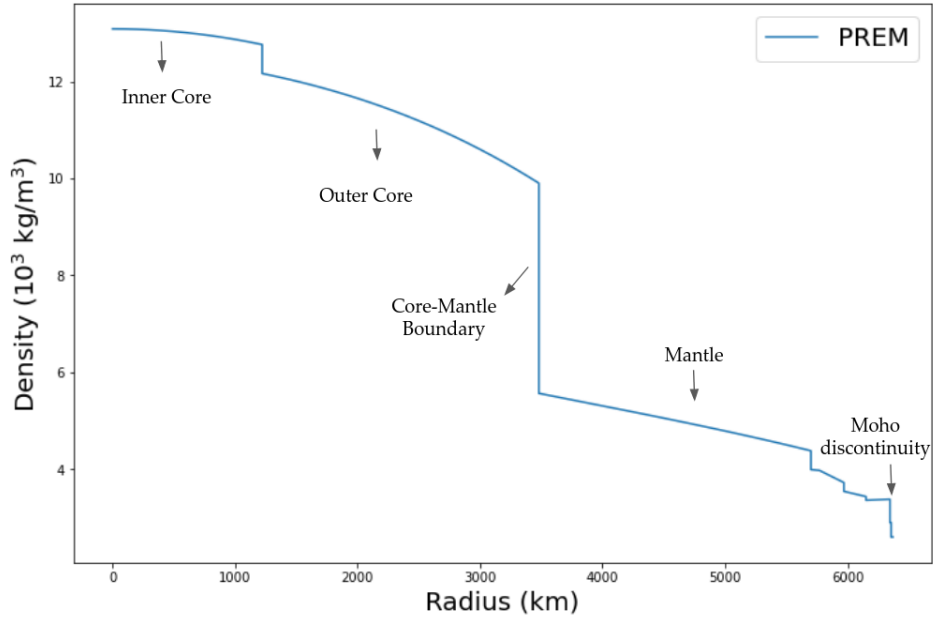


Figure 2.4: PREM model of Earth's internal structure

The metallic core, segregated during the primary evolution stage of a primitive magma ocean, is composed mainly of Fe and Ni in chondritic proportions (Lichtenberg et al., 2022). The physical properties of sub-regions in the mantle are mainly controlled by the compositional changes or phase changes with depth. (Ringwood, 1991) described how the upper mantle consists of olivine, two parts of pyroxenes and garnet following a **pyrolitic** composition based on the relation-

ship between basalts and peridotites for estimating major and minor elements in the mantle.

On geodynamical evolution models, there's a zone described by a discontinuity between 410 and 660km, with different mineralogy and a strong seismic velocity gradient known as **transition zone** Ringwood (1994). Samples from this region have been found as inclusions in diamonds and some fragments in kimberlites (Smith et al. (1984); Moore and Gurney (1985); Sautter et al. (1991); Kesson et al. (1994); Harte and Harris (1994)). Moreover, we have been able to retrieve samples from all the zones described before in the mantle, the upper mantle is the one that provides geologists with the largest amount of samples through magmas that bring xenolith fragments to the surface, or through tectonic processes.

2.2.2 Governing equations for mantle convection

Heat can be transported from the hot metallic core to the surface by two main mechanisms: Conduction or convection, with convection being the most efficient one through the whole mantle. The vigor of convection influences the effectiveness of cooling and partial melting within the silicate mantle, which drives the crustal formation and volcanic gas release (Turcotte and Schubert, 2002). As a result, internal dynamic processes can be connected to surface phenomena like tectonics, volcanism, and the development of the atmosphere. This section will review the theory behind mantle convection, the governing equations, the important factors controlling plate motion on Earth, and how to extrapolate this knowledge to exoplanets.

Thermodynamics-Mantle as a fluid

As mentioned before, we know that near-surface regions show elastic behavior. Consequently, to compensate for stresses from this thin layer, the deeper rocks must behave as a fluid in geological time scales (Turcotte and Schubert, 2002). In this way, the temperature describes the rheology (study of flow and deformation of materials under applied forces or stresses) of the silicate mantle as a function of depth. This temperature will be affected by the heat transfer mechanism working inside the planet.

As we consider the mantle a non-static fluid in geological timescales, some mathematical formalism can describe and assure that the physics behind the mantle dynamics is consistent. This means that all assumptions must follow the conservation of matter and energy together. In this way, we can think of the motion of a fluid described by the motion of infinitesimal elements. Let us suppose we want to study the velocity field of a fluid. In that case, we are referring to the velocity at a given time t of every element, which means that the element of the fluid is moving along with the fluid. The Eulerian formalism gives

the total time derivative of the velocity:

$$\frac{dv}{dt} = \frac{\partial v}{\partial t} + (v \cdot \nabla)v \quad (2.1)$$

On the other side, if we consider the derivatives from the point of view of particles moving with the fluid, we can describe them with the Lagrangian formalism:

$$\frac{D}{Dt} = \frac{\partial}{\partial t} + u \cdot \nabla \quad (2.2)$$

We can make an analogy with traffic flow for easy understanding: we can study the system in terms of the density of cars ρ and their velocity on the road, v . We use the Eulerian formulation to describe the density and velocity as a function of a fixed position on the road. Still, if we describe it from the point of view of the drivers, we are then using the Lagrangian formalism.

Now that we know the different ways of describing the state of a fluid, we can introduce the physical background that makes sense when talking about the mantle as a fluid. We can describe the mass flux moving through a closed surface S such that:

$$\frac{dM}{dt} = \oint \rho v dS$$

The decrease per unit time in the mass is:

$$\frac{\partial}{\partial t} \int \rho dV = - \oint \rho v dS \quad (2.3)$$

It's the integral of a divergence over the volume, which lets us use Gauss' theorem:

$$\rho v dS = \int \nabla \cdot (\rho v) dV \quad (2.4)$$

$$\int \left[\frac{\partial \rho}{\partial t} + \nabla \cdot (\rho v) \right] dV = 0 \quad (2.5)$$

This must be true for any volume, so the integral must be zero too, which brings us to the Eulerian form of the equation of continuity where ρv is the mass current or mass flux density:

$$\boxed{\frac{\partial \rho}{\partial t} + \nabla \cdot (\rho v) = 0} \quad (2.6)$$

Which is the equation for the **conservation of mass**. Now, let us consider a moving fluid element from the Lagrangian point of view. The change of momentum of the particle per unit volume is given by:

$$\rho \frac{dv}{dt} = \rho \left(\frac{\partial v}{\partial t} + (v \cdot \nabla)v \right) \quad (2.7)$$

From Newton's law, all the forces acting on this fluid element must be equal to the rate of change of momentum. If we only take the force acting due to pressure:

$$-F_P = \oint p dA \quad (2.8)$$

The negative sign is because the force is directed towards the increasing pressure direction such that:

$$-F_P = \int_V \nabla P dV \quad (2.9)$$

$$\boxed{F_P = -\nabla P} \quad (2.10)$$

$$\rho \frac{dv}{dt} = -\nabla P \quad (2.11)$$

$$\rho \left(\frac{\partial v}{\partial t} + (v \cdot \nabla)v \right) = -\nabla P \quad (2.12)$$

This brings us to Euler's equation for the **conservation of momentum**:

$$\boxed{\frac{\partial v}{\partial t} + (v \cdot \nabla)v = -\frac{1}{\rho} \nabla P}$$

Including gravity, we have:

$$F_g = -\rho \nabla \phi \quad (2.13)$$

So, Euler's equation became:

$$\frac{\partial v}{\partial t} + (v \cdot \nabla)v = -\frac{1}{\rho} \nabla P - \nabla \phi \quad (2.14)$$

In this whole derivation, we assumed an ideal fluid, meaning that it's not losing energy in terms of viscosity, conduction, dissipation, etc. But, as we are studying the mantle as a realistic case, it is necessary to add a viscosity term, that

describes the friction acting against the acceleration of the fluid element. The full equation that incorporates those terms is called: **Navier-Stokes conservation of momentum equation**

$$\boxed{\frac{\partial v}{\partial t} + (v \cdot \nabla)v - \nu \nabla^2 v = -\frac{1}{\rho} \nabla P + g} \quad (2.15)$$

With ν being the viscosity of the mantle. From these previous constitutive laws, we can derive the energy conservation equation knowing that the total energy of the fluid is given by $E = u + \frac{v^2}{2}$, with u being the potential energy and v the factor associated to the kinetic energy. This total energy can change in time due to several factors, such as: an advection term that describes how the energy is moving along the fluid, transfer of energy through the surface element without mass transport, work done by body forces, work done by surface forces and the internal heat production. Obtaining the final form of the energy conservation equation:

$$\boxed{\rho C_p \left(\frac{\partial T}{\partial t} + v \cdot \nabla T \right) - \nabla \cdot (k \nabla T) = \rho H + \alpha T (v \cdot \nabla p) + 2\nu \dot{\epsilon} : \dot{\epsilon} + \rho T \frac{DS}{Dt}} \quad (2.16)$$

With C_p , $\dot{\epsilon}$ and $\frac{DS}{Dt}$ being the specific heat, the stress tensor, and the term associated with the enthalpy, respectively. The left-hand side of the equation contains the terms corresponding to the change of thermal energy, convection, and conduction. At the same time, the right-hand side of the equations describes the internal energy production, adiabatic heating, shear heating, and latent heat. Now that we know which equations are used to solve geodynamical problems, we can start talking about approximate equations derived from the general form of the constitutive laws. The one that we are interested in is the **Anelastic liquid approximation**. This re-formulations of the conservation equations sets the mass conservation approximation to a reference density profile such that:

$$\nabla \cdot v = -\frac{1}{\bar{\rho}} \frac{\partial \bar{\rho}}{\partial z} \frac{g}{\|g\|} \cdot v \quad (2.17)$$

Where the reference profiles for the density $\bar{\rho}$ and the density gradient are introduced by the adiabatic conditions model, in this case, given by the user through temperature, hydrostatic pressure, and density profiles. This approximation is used with a material model that defines a temperature-dependent density.

This brief description of equations is the one that ASPECT ([Bangerth et al., 2022a](#)) solves in 2D/3D for Earth's mantle convection problems used during this

thesis. In this way, to be consistent with simulations, the constants in conservation equations described before must be coherent regarding the unit system, independent of which one the user would like to use. Consequently, for software like ASPECT, it is feasible to implement the geometry and material models such that all parameters are normalized. This simplifies, for example, simulations run over a parameter space, where we introduce non-dimensional numbers with differences on several orders of magnitude through normalized constants to map the main effects on each case.

One of those non-dimensional numbers is the Rayleigh number, a parameter that quantifies and describes how vigorous the convection is within a system. It is described by the ratio of convecting driving forces to resisting forces (Turcotte and Schubert, 2002). In other words, the comparison between the conduction and advection time. Let's consider a parcel of a mantle, which in geological timescales is a fluid parcel. The velocity of the parcel is described by:

$$v \approx \frac{\Delta \rho g L^2}{\nu}$$

Where ρ is the density of the silicate mantle, g is gravity, L is the thickness of the layer, and ν is the dynamic viscosity. Consequently, the advection time is:

$$\tau_a = \frac{L}{v}$$

Comparing to the conduction time, we arrive at the final expression of the Rayleigh number:

$$\tau_c = \frac{L^2}{\kappa}$$

$$Ra = \frac{\tau_c}{\tau_a} = \frac{vL}{\kappa} = \frac{\rho \alpha g \Delta T L^3}{\kappa \nu}$$

With α being the coefficient of thermal expansion, ΔT is the thermal difference between the top and bottom of the convecting layer, and κ the thermal diffusivity. For generating a convective instability in large scales, a critical value of Ra must be reached, ($Ra_{critical}$), which, as mentioned before, will depend on the geometry of the problem and the boundary conditions imposed (Rolf et al., 2022). Some estimates at the Earth's lower mantle put this non-dimensional parameter at $Ra \approx 10^7$ - 10^8 (Turcotte and Schubert, 2002).

2.2.3 Heating sources and partial melting

Heat sources in a planetary mantle contribute to the planet's overall heat budget. The primary sources include:

- **Accretional energy:** Heat released from the hot core due to planetary accretion and differentiation processes.
- **Adiabatic:** When convection occurs within the mantle, upwelling structures bring material from the bottom of the layer (high P and T) to regions of lower pressure, allowing decompression. As a result, adiabatic heating describes the thermal profiles of the mantle. Producing topography at the boundaries of the convective cells ([Rolf et al., 2022](#))
- **Radiogenic:** Heat released due to the decay of radioactive elements. For instance, partial melting will precipitate elements like U,Th,K and Al, as they are incompatible and will end up mainly in the crust. The volumetric heating generated by these isotopes, combined with the gradual cooling of the Earth, facilitates the process of mantle convection.
- **Shear:** Viscous flow occurring within the Earth serves as a mechanism for heat dissipation. In this process, the kinetic energy associated with the flow is transformed into thermal energy, converting mechanical energy into heat.
- **Tides:** Heat produced by the tidal forces exerted on a celestial body. In exoplanets, this is an important feature as some systems show very close orbital distance, and due to these forces, they will tend to circularize their orbit and synchronize it with their spin.

More existing heating sources, both internal and external, contribute to the Earth's overall energy budget. Nevertheless, the ones described before are the main ones when producing geodynamical models on Earth's mantle convection problems.

Transfer mechanism

As discussed before, due to the thermal gradient between the Earth's hot core and the surface, there are different ways to transport heat within Earth's mantle. Depending on the rheological properties of the rock, one mechanism will govern over the others. And, in some cases, they co-exist on local scales. In this case, for geodynamical problems, we consider these two main mechanisms:

- **Conduction:** In a diffusive process, molecules transmit their kinetic energy to other molecules by colliding with them. Heat is conducted through a medium that exhibits spatial variations in temperature. This mechanism works in the

lithosphere, for instance, the upper boundary layer of a nominal thermal profile of Earth's mantle.

- **Convection** This mechanism is associated with material motion within a system. For example, when a fluid is heated from below and cooled from above in a system with a gravitational gradient (like in the case of Earth's mantle), thermal instabilities will start rising, letting convection happen. In this way, colder and denser rocks from the lithosphere descend into the mantle, and hotter material ascends to the surface.

Adiabatic temperature profile

A system describing convection with a $Ra > Ra_{critical}$ develops thin **thermal boundary layers (TBLs)** at the top and bottom of the system, where the heat will be transported mainly by conduction, but due to the constant influx of heat into these layers, there will produce convective instabilities, expressed as **upwellings and downwellings**. The larger the Ra , the thinner the TBLs (Rolf et al., 2022).

On Earth, the surface temperature is around 300 K. In contrast, the temperature within the adiabatic mantle reaches approximately 1600 K at the bottom of the lithosphere. This temperature disparity stems from the fact that the bulk of the mantle is in thermal equilibrium, exhibiting a thermal profile that aligns with the latter temperature. On the other side, the significant difference between the actual surface temperature, which is relatively low, and the exceedingly high temperature at the core-mantle boundary induces a thermal boundary layer, as explained earlier. A typical adiabatic profile is shown in Figure 2.5.

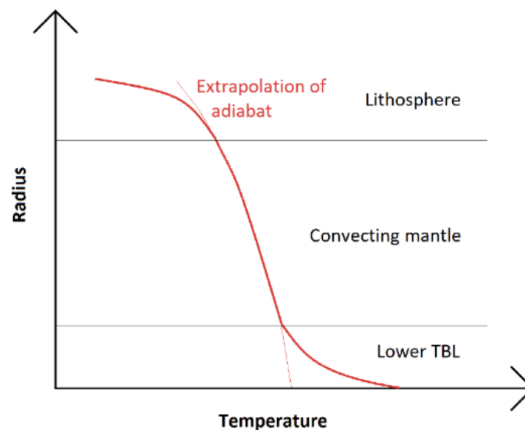


Figure 2.5: Illustration of an adiabatic thermal profile in the mantle. Two boundary layers are described at the top and bottom of the system, where the heat is carried by conduction.

Partial melting

Melting is a first-order phase transformation that has drastic consequences for various geophysically observable material properties. Partial melting in the mantles of telluric planets results in magma formation. It is the surface movement and eruption of these magmas that are responsible for surface volcanism, serving as a critical connection between mantle dynamics and the overall composition of the planet. In a multiphase assemblage, melting begins once the system or parts of it reach a specific temperature at which liquids form. This is known as **solidus**, and once the temperature is higher, it reaches what is known as **liquidus**, the temperature at which the last crystal melts. Melting allows massive outgassing of volatiles (Katz et al., 2003). This process can take place in different geodynamic contexts as described in Figure 2.6. We call **fractional crystallization** the process where minerals with different melting temperatures precipitate and are removed from the assemblage, which gives. As a result, a different residual magma composition (Lichtenberg et al., 2022). The variation in melt fraction is believed to be influenced by the solidus and liquidus temperatures, which depend on pressure and composition. In silicate systems, volatiles like H_2O and CO_2 can lower melting temperatures. When silicates are saturated with water or CO_2 , the solidus temperatures can be reduced by a significant amount, ranging from 600 to 800 K (Dasgupta et al., 2007).

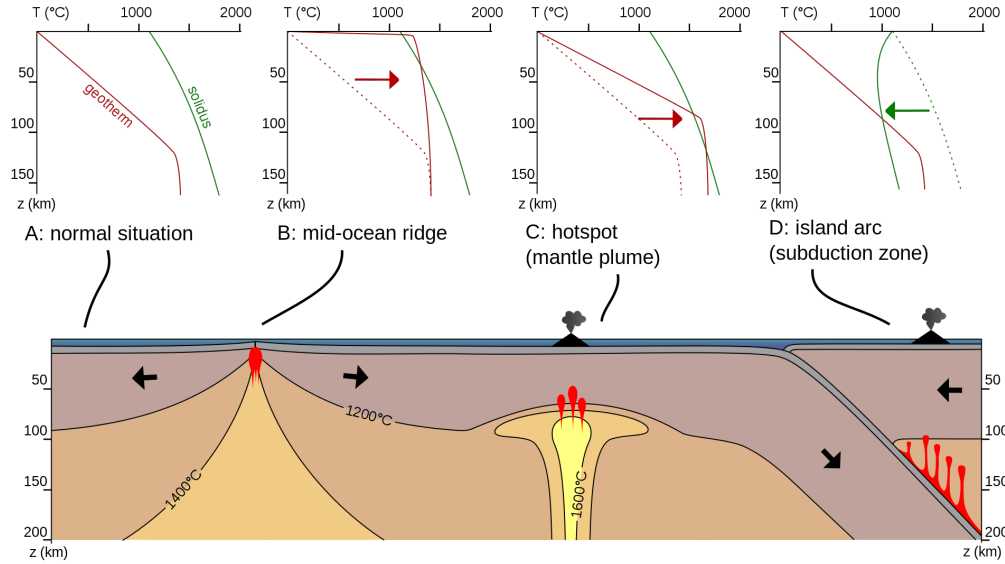


Figure 2.6: Illustration of different geotherms according to the partial melting processes that give rise to the generation of magma as a function of depth. Plot from Grotzinger and Jordan (2010)

To consistently model solid and fluid/melt processes is necessary to implement a parameterization of mantle melting that includes the effects of significant amounts of water. In this study, we are following the parametrization implemented by [Katz et al. \(2003\)](#) where:

$$T_{solidus}(P) = T_{solidus}(P) - \Delta T(X_{H_2O}) \quad (2.18)$$

In this context, $\Delta T(X_{H_2O})$ represents the temperature reduction experienced by the solidus due to a specific water content present in the melt.

Geodynamics and compositional variation

At depth, mantle rocks experience phase transitions that modify their mineral composition depending on the P-T conditions. These transformations change the density and viscosity, facilitating the layering within the mantle ([Weidner and Wang, 2000](#)). While the planet's formation stage primarily influences the overall composition, heterogeneity can arise from melting and cooling processes. Different rock compositions melt under different conditions and show different partitioning into the molten phase ([Hofmann, 1997](#)). In this way, convection tends to homogenize lateral variations. Nevertheless, the timescales for mixing in the mantle are very large, and compositional heterogeneity will likely exist across multiple scales in the present-day Earth's mantle ([Fontaine et al., 2015](#)).

Furthermore, these processes generate secondary renewed crust as they occur in the upper mantle, letting this melt to cold down and crystallize. In that way, once the melt is produced, there's a latent heat consumption and an eventual release to the surface. Which makes partial melting as a crucial event for the cooling process of a rocky planet. (e.g., [Ogawa \(2000\)](#); [Ogawa and Yanagisawa \(2014\)](#); [Lourenço et al. \(2016\)](#))

2.2.4 Planetary geodynamic regimes

The geological evolution of telluric bodies is determined by the heat generated within them and how it is dissipated toward the surface ([Rolf et al., 2022](#)). The main regimes we're interested in are the **mobile lid** and **stagnant lid** described, for instance, on the Earth and Venus (Figure 2.7). The first one consists of the specific behavior within the upper thermal boundary layer in continuous motion and which velocity is higher than the average convection velocity. [Tackley \(2000\)](#) defines this surface mobility M as the ratio between surface-averaged to volume-average velocity to distinguish between both regimes. **Plate tectonics** is one expression of this kind of mobility. It is characterized by the significant surface movement of lithospheric plates, continuously deformed, cooled, and recycled in the mantle. This plate tectonics regime is characterized by high average surface

heat flow, mainly concentrated along the constructive plate boundaries, resulting in efficient planetary cooling.

Conversely, in the stagnant lid regime, the heat is thought to be dissipated mainly by conduction through the thick lid, leading to low heat fluxes (Solomatov and Moresi, 1996). That means that the crust will show a rigid behavior with respect to the flowing mantle convection in geological time scales. This regime can also be interpreted as the final stage of mantle convection when the planet is cooling down enough to stop the convection slowly (O’Neil et al., 2016). In this regime, when stresses in the crust overcome its internal strength locally can bring the material to break and start subduction. In this classification, as heat transfer to the surface is inefficient, melting and latent heat consumption at the bottom of the lithosphere must be released through localized magmatism, reducing the mantle’s temperatures (Ogawa and Yanagisawa, 2014). Figure 2.7 shows this dichotomy between regimes.

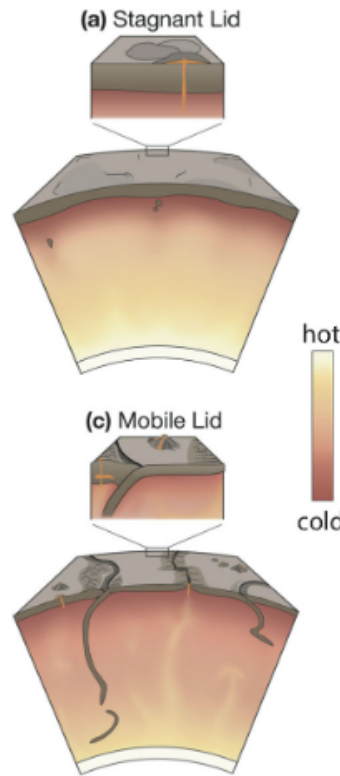


Figure 2.7: Schematic illustration of two modes of mantle convection produced by Rolf et al. (2022). Mobile lid activity on Earth is characterized by plate tectonics while on Venus is considered to be Stagnant-lid over the last ≈ 500 Myrs (Solomatov and Moresi (1996)).

When we are talking about exogeodynamics we are referring to the study of internal dynamics of rocky exoplanets. One important feature the exoplanet community is investigating today is plate tectonics's **likelihood**. Many studies have tried to understand this problem. For example, [Noack and Breuer \(2014\)](#) describes the likelihood of plate tectonics based on different core-mass fractions depending on the wet or dry rheology. This likelihood is computed according to the stresses present in the crust and the model used. These stresses can be measured through the **yield stress**, defined as the maximum stress a material can sustain without deforming plastically. For plate tectonics to operate and maintain is necessary that the stresses at the lithosphere are around 100MPa depending on the mass distribution and the crustal thickness ([Karato and Barbot, 2018](#))

Methodology

3.1 Computation of the internal structure

In this section, I will discuss the methods used to perform a parameter study to identify the conditions that favor the melting presence and the mobile-lid regime in these planetary bodies. I modeled the heat transfer in the mantles of Earth-sized exoplanets for various internal structure configurations in terms of the relative size of the core compared to the mantle. On Earth, many rheological properties are described by the effects of thermodynamic equilibrium of mineral phases at different P-T conditions. To be consistent, we replicate the same surface conditions in every simulation to compare with the geophysical properties of our planet.

3.1.1 Silicate mantle composition

As mentioned, it is possible to constrain the internal structure from observations regarding mass, and density. As we have no clue about the composition distribution of the interior of these planets, as a first approach, we assume a fixed Earth-like rock composition for all the planets we are simulating. For this purpose, we use the tool *PerpleX* ([Connolly and Petrini \(2002\)](#); [Connolly \(2005\)](#); [Connolly \(2009\)](#)), which lets us compute the self-consistent composition phase diagram. This type of diagram shows the phase relations of a closed system as a function of independent variables (P-T).

In this case, we model the silicate mantles assuming a pyrolitic composition likely to Earth's upper mantle, following the composition proposed by [Stixrude and Lithgow-Bertelloni \(2005\)](#). This way, we compute self-consistent phase equilibrium and physical properties of a **pyrolitic** mantle under conditions that go from 0.0001-140GPa and 300-3800K. This means that we assume a homogeneous mantle that goes from the Core-Mantle Boundary (**CMB**) until the planet's surface.

3.1.2 1D-references profiles computation for Earth-like planets

We can think of a rocky planet structure as an ‘onion’ with density-stratified layers that extends from the center with a liquid metallic inner core, followed by a silicate mantle and a crust. In a 1-D multilayered model, physical properties such as pressure, gravity, temperature, and temperature gradient must be continuous throughout the whole planet profile. To ensure this continuity, we used the open-source software BurnMan (Myhill et al. (2022); Cottaar et al. (2014)), which lets us calculate the physical and chemical properties of fluids/melts, solutions, and composite assemblages. Solving the Birch-Murnaghan finite-strain EoS (Stixrude, 2002), BurnMan can compute the bulk modulus, shear modulus, and density, depending on the surface temperature.

Metallic core

On Earth, the metallic core is subdivided into solid/liquid phases. Although, for exoplanets, we have no clue that this is also true. In this way, we assume that all planets simulated here have a single liquid core with the following molar composition (Fe: 90., Ni: 5., Si: 2., O: 3.), ignoring Carbon and Hydrogen according to Zhang et al. (2021). Assuring that the temperature mode for this layer is completely adiabatic, we extend the inner core from the center to the **CMB** depending on the case following the hydrostatic equilibrium equation:

$$\frac{dP}{dr} = \frac{-GM(r)\rho(r)}{r^2} \quad (3.1)$$

As we want to explore all the parameter space on the internal structure of this planet, we vary the core size at the same time, we vary the Fe and Si content to be able to reproduce the exact mass and radius of the Earth.

Mantle

Secondly, we used the material properties computed with **PerpleX** before and created a layer that goes from the CMB to the bottom of the lithosphere. For this 1-D profile, we assume a single mantle layer convecting with a $Ra=1e7$. This layer is defined in such a way that it follows a perturbed adiabatic temperature profile and describes thermal boundary layers at the upper and lower mantle. Finally, we add a linear term of super adiabaticity described by Anderson and Dziewonski (1982) to the temperature profile settled at the lower mantle. This, follows the PREM model (Dziewonski and Anderson, 1981) used for the Earth and has been corroborated on seismic tomographies.

Core-Mantle Boundary configurations

As mentioned before, the level of degeneracy on the internal structure of exoplanets is very high as we don't have direct proxies to measure it from direct observations. To tackle this statement, we iterated over all possible combinations of Fe, Si and CMB in the core, that match the mass and radius of the Earth. For that purpose, we define the minimum core size as 0.5R (Earth configuration) and the maximum as 0.9R (corresponding to the biggest core case in the Solar System (Mercury)). Also, we assume a single liquid metallic core.

CMB	Distance from the center (km)
0.5R	3185
0.6R	3822
0.7R	4459
0.8R	5096
0.9R	5733

Table 3.1: Radial distances for the different core sizes configurations selected for 1-D and geodynamical simulations.

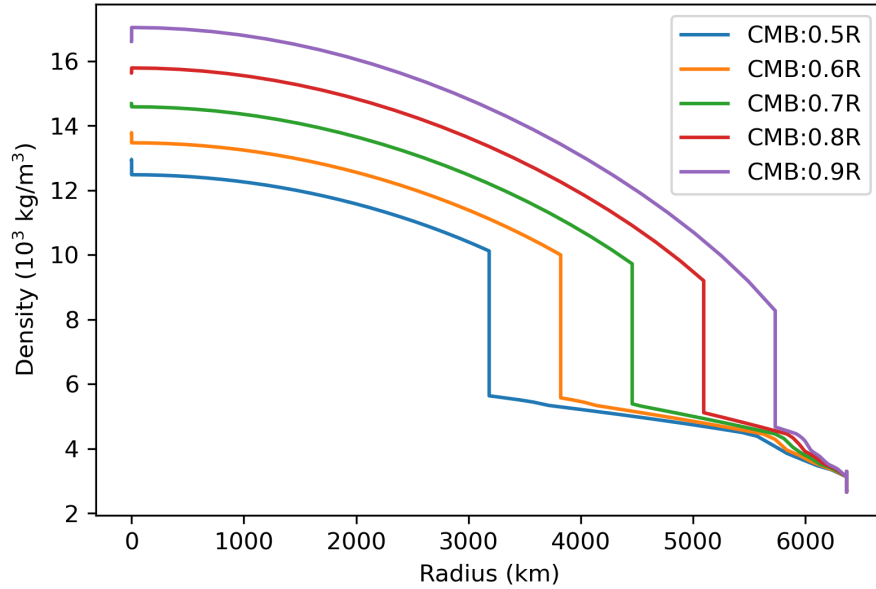


Figure 3.1: Density profiles for Earth-like exoplanets for five different CMB configurations reproducing the same mass of the Earth.

3.1.3 Trappist-1 planets modeling

We first calculated a 1D “Earth-like” temperature, density, pressure and viscosity profile, which corresponds here to the internal structure the planets would have if they had the same composition as the Earth for the outer core, mantle, and lithosphere. The latter one, is assumed to have a dunite composition with a thickness of 200km.

Assuming initial temperatures of 300K at the surface, 620K at the moho discontinuity, and 1550 K at the top of the mantle, we proceeded to explore various scenarios by altering the iron (Fe) and silicon (Si) content in the planetary cores. These scenarios included the smallest possible core with the highest iron content, the largest possible core with the lowest iron content, an intermediate case, and a case resembling Mercury (where the core-size ratio is 85%). It is important to mention that the largest core case surpasses the maximum core size observed in the solar system. This is precisely why we also consider the Mercury-like case as a reference point.

Additionally, we accounted for different surface temperatures across all planets, specifically 300K, 600K, 800 K, and temperatures more representative of each planet’s surface. The changes in surface temperature were also applied to the moho and lab temperatures, maintaining consistency. For each surface temperature, we calculated the composition to replicate the various core-mantle size ratios mentioned earlier. As temperature directly affects the internal structure, the resulting core compositions differed for each surface temperature.

3.2 2-D mantle convection simulation using ASPECT

Initially, computations were done using the ASPECT code version 2.4.0, see (Kronbichler et al., 2012; Heister et al., 2017; Bangerth et al., 2022a,b; Rose et al., 2017; He et al., 2017). Depending on the case, the initial values on the input file are going to define how complex and realistic is the situation that the software is simulating. In this section, I will explain the different parameters chosen for this kind of geodynamical scenario and how we approximate Earth values for rocky exoplanets.

3.2.1 General set up and initial conditions for geodynamical simulations

First, using the temperature, pressure, and density profiles extracted from the 1-D models presented before, I defined the material model as a -Reference model- which means, that all the adiabatic conditions are following the 1-D profiles computations. For this kind of configuration, I used the **anelastic liquid approximation** described in the second chapter of this thesis. In the case of the

Earth, we have paleomagnetic data that let us identify the velocity and direction at which tectonic plates are moving. As we don't have access to that information for exoplanets, I decided to use boundary conditions that let the velocity be tangential to the surface and zero at the inner boundary, which is the CMB. This means we are implementing a free-slip condition.

Secondly, we set the age of the top boundary layer as $5e7$ yr, which is the standard time to treat these geodynamical problems as a solid-state convection scenario. In the energy equation described in Section 2.1, the coefficients that describe the heating mode on each simulation are the heating sources of each exoplanet. As we explored the whole parameter space, we included three sources: radiogenic, shear, and adiabatic heating. For a comparison method, we run all simulations with each mode separately and then all combined to compare each contribution separately.

The initial conditions were retrieved from the reference profiles for the adiabatic and shear heating. In the case of radiogenic heating, we divide the mantle into two zones: above and below 300km from the surface. Each zone is described as a compositional field advecting with two radioactive elements, in this case, U^{238} , Th^{232} . Setting the specific half-decay times, heating rates, and initial concentrations of each element in each zone, it was possible to make an analogy with Earth's radioactive heat budget. Once again, we don't know how these elements are distributed along the isentrope for exoplanets, especially for the different internal structures we are simulating. Thus, we re-scaled the original values of heating rates in the mantle and crust from the Earth, accordingly, the volumetric change between CMB configurations.

We study the different cases of CMB configuration and Ra number for each heating budget. This parameter described in Section 2.2.2 will give us information on how vigorous the convection is in the mantle configuration chosen. As a mathematical trick, we introduce this parameter via the gravity value, taking advantage of the non-dimensional equations we are using. Several estimates put Ra in the lower mantle at $Ra = 1e7$ on Earth. The explored configurations in terms of Ra and CMB ratios are displayed in Table 3.2.

Ra/CMB	0.5R	0.6R	0.7R	0.8R	0.9R
10^2	0.000981	0.000981	0.000981	0.00981	0.0981
10^3	0.00981	0.00981	0.00981	0.0981	0.981
10^4	0.0981	0.0981	0.0981	0.981	9.81
10^5	0.981	0.981	0.981	9.81	98.1
10^6	9.81	9.81	9.81	98.1	981
10^7	98.1	98.1	98.1	981	9810

Table 3.2: Input parameter values of gravity for all simulations to introduce the respective Ra number.

As this model requires solving the fundamental equation 2.16 in a 2-D mesh, the most comfortable choice is to run the simulations in parallel. This means ASPECT will solve the whole mesh in time, subdividing the work into different CPUs. This reduces the time considerably. For this reason, we use the super-computer system of the University of Geneva -Yggdrasil-, where each simulation was run with 30 cores for a maximum time limit of 50hr. This is to ensure the convergence of each simulation as a final state. Now, this convergence is measured according to the average temperature evolution during the whole running time. Once it arrives at a constant temperature, it is possible to say that we are in a steady state (Figure 3.2)

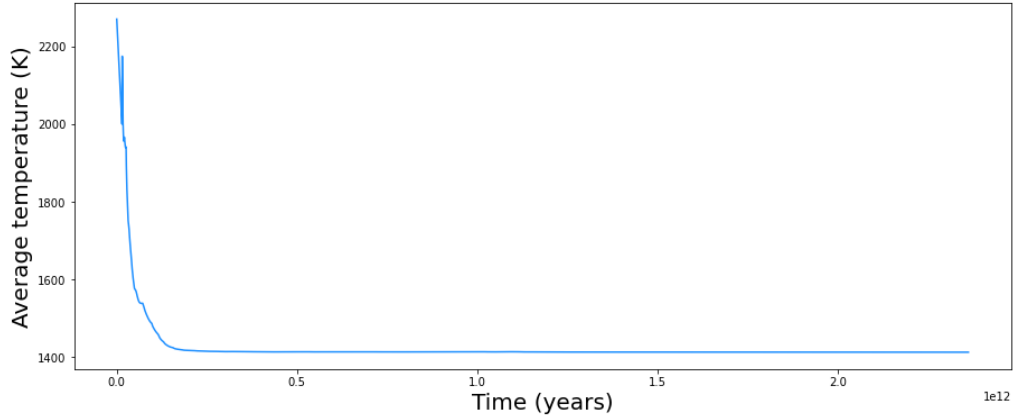


Figure 3.2: Average temperature of a simulation describing the CMB configuration $\approx 0.5R$ and $Ra \approx 1e7$, this example just includes the adiabatic heating in the energy equation. The vigor of convection will be proportional to the convergence times in all cases.

For simplicity and to reduce the computation time, we choose a geometry of a quarter of a ring (illustrated in Figure 3.3). When exploring the whole parameter space, we vary the vigor of convection. In that way, large Ra numbers will give rise to structures of the flow smaller and more chaotic. That means, if the mesh is not well defined in every situation is not possible to accurately resolve these plumes in the advecting field, and it is necessary to refine it even more. For this reason, we chose to use an adaptative grid. This 2-D grid, where the equation solver is working, will change every certain time step depending on the error computed in the previous time step on every cell. Thus, we can avoid any kind of convergence problems during the process. Also, we decided to explore from $Ra = 1e2$ to $Ra = 1e7$, because for larger Ra , the detail required was outside too high, implying more CPUs time and refinement, and we were not interested in the detail on time for every plume or local process.

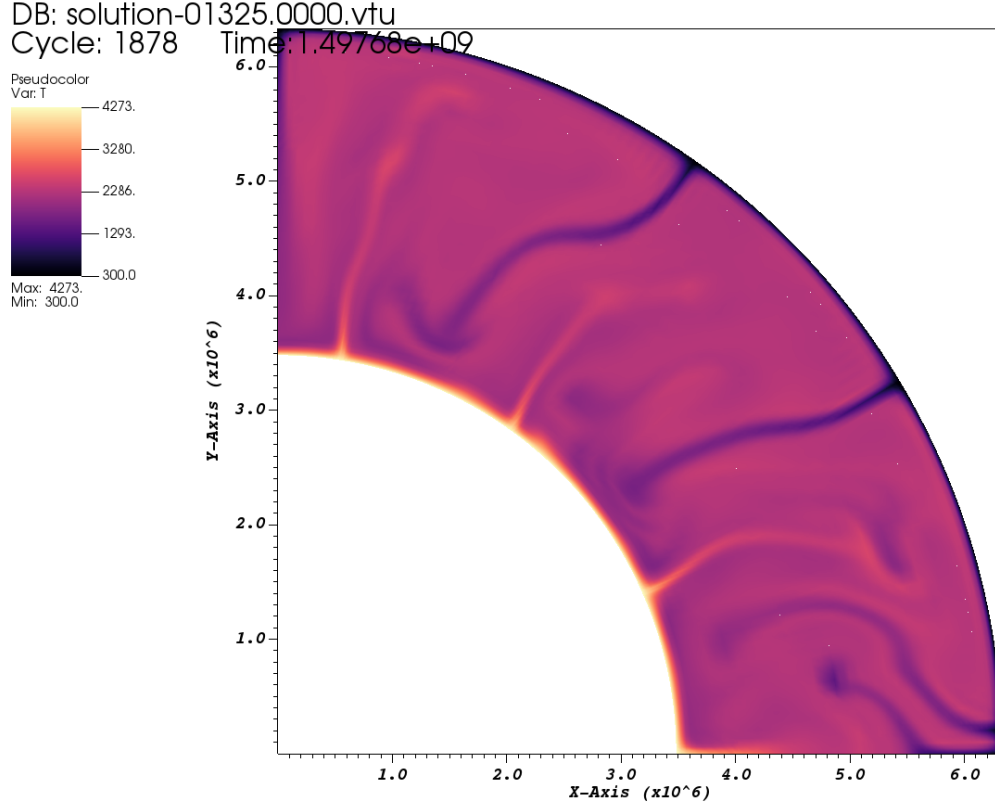


Figure 3.3: Example of a convective simulation with CMB configuration of $0.5R$ and $Ra=1e7$. The inner and outer temperatures are described by the heating from the core and the respective surface temperature, which in this case, is set for all simulations at 300K.

3.2.2 Thermal-lid thickness

Once we've run the different simulations and know they are in a steady state, we look into the profiles that show a **convective** behavior. As explained, in the Theory section, the conductive profile will linearly increase the temperature with depth. In contrast, the convective profile will display thermal boundary layers at the top and bottom of the system. The next step is to find the lid thickness. For this purpose, we plot the different temperature profiles along the mantle and then extract the inflection point of the upper thermal boundary layer. We compute this, finding the second derivative of the curve in the first 300km. Consequently, we can find the intersection of this point with the y-axis, which is the value we are looking for. On Earth, this lid is described as the base of the asthenosphere, where there's a difference in the physical properties of the rock, and it gradually transitions into a conductive layer which is the case in the crust.

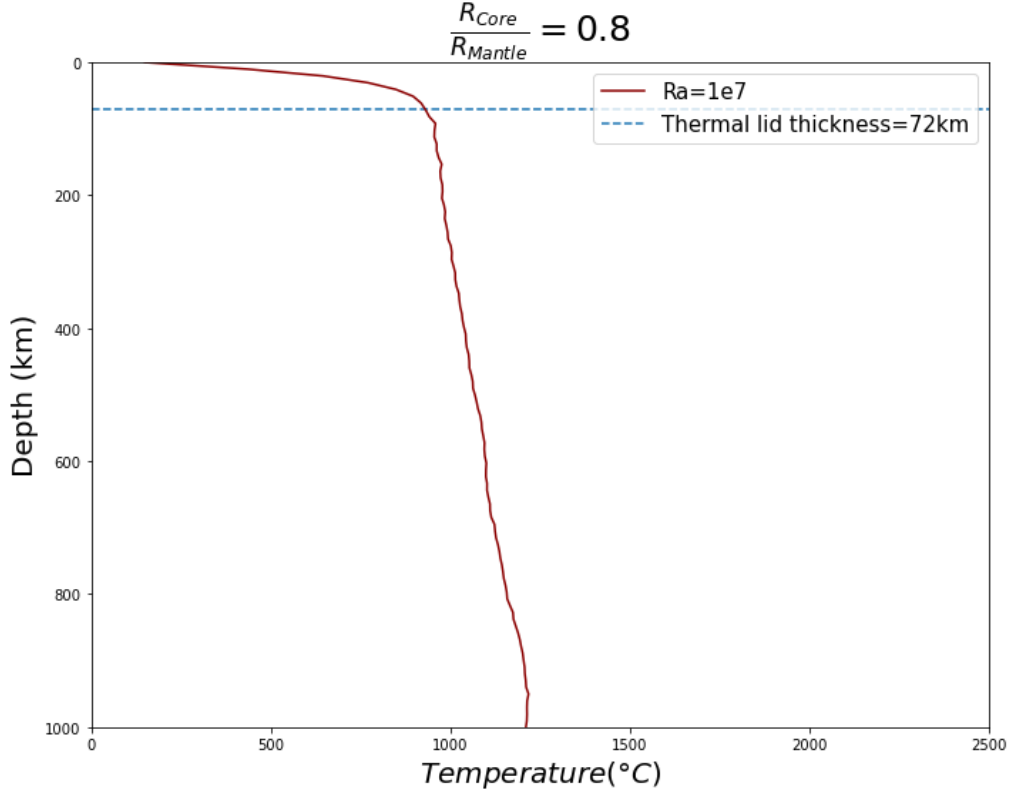


Figure 3.4: Adiabatic profile for the first 300km in a CMB configuration 0.8R and $Ra=1e6$, the thickness of the thermal lid is defined, finding the second derivative of the adiabat.

3.2.3 Melting values computation

Furthermore, the next step is to compute the amount of melt available in every case of the parameter space. Consequently, we can find the amount of water that every configuration can produce according to the heating mode. Thus, if actual observations show a higher amount of water vapor in the atmosphere of exoplanets, we can imply that external events are producing these extra values, like, for example: **-volcanism induced by tectonic activity-**. For this purpose, the parametrization proposed by [Katz et al. \(2003\)](#) was used, for the range between 0-10Gpa, which is the range we are interested in, as we are looking into the possible internal structures that can produce melt at the lithosphere region. Depending on the geotherm and every case of heat source, we can integrate the area between the geotherm and the solidus for different bulk water contents of the system. Finally, we can compute the volumetric amount of water in spherical coordinates, and that should be the normal amount of water released in a non-tectonic plate planet.

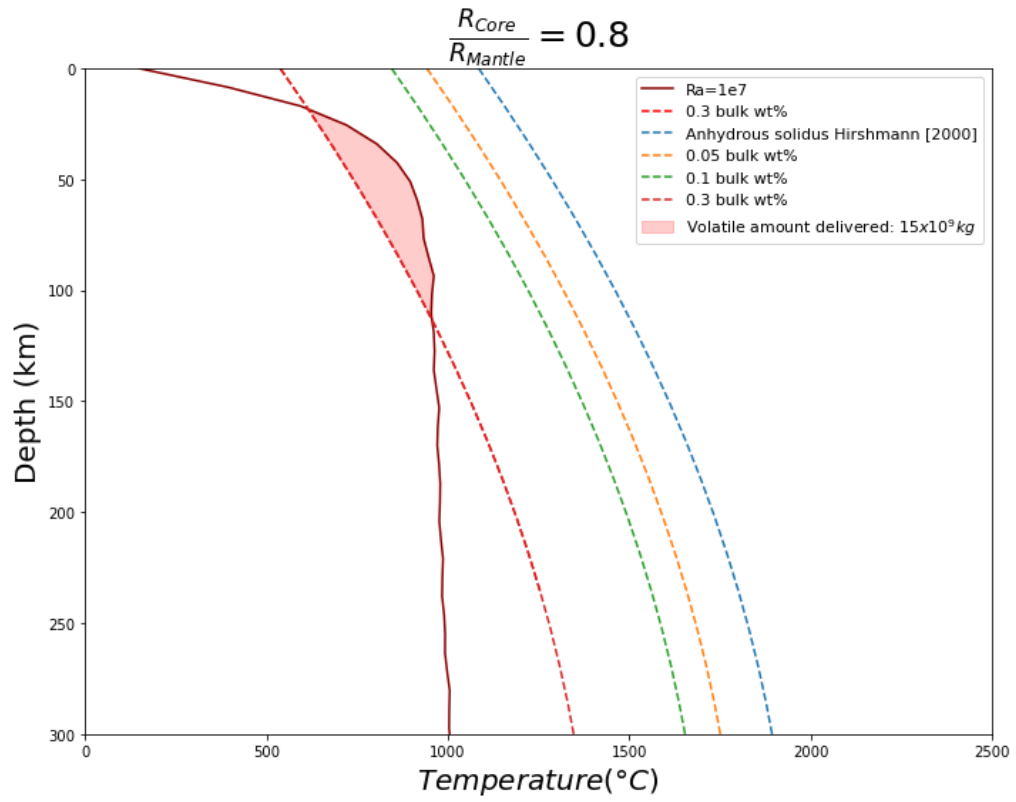


Figure 3.5: Temperature profile of a planet with CMB configuration of $0.9R$ and heating mode set as only adiabatic. In this case, the geotherm only intercepts the solidus temperature for a system with 0.3 bulk wt %.

Results

4.1 Temperature profiles

Initially, we run all the simulations into the whole parameter space described before. We started just adding into the energy equation the term of adiabatic heating from the 1-D profiles extracted from BurnMan. Depending on the Ra number and the CMB configuration, it's possible to observe in the visualization post-processor different features during the long-term evolution and distinguish between a convective and a conductive behavior. The first one sketches a conductive transfer mechanism during the first million years and, consequently, the rising of Rayleigh-Taylor instabilities that rises from the bottom of the mantle to the surface; we know them as plumes. The more complex and chaotic the structures, the more it takes to converge into stable convection, and more computational time is required.

For each simulation, I extract the heat flux statistics, temperature as a function of depth, and the root mean square velocity of the flowing mantle. The typical steady-state temperature profile displays a well-mixed model with a hot inner and cold outer boundary with a constant temperature with thin boundary layers at the bottom and top of the mantle. Figure 4.1, shows how both regimes are characterized in this profile. For the conductive regime, there's a linear increase of temperature with depth, which is the case for the lower Ra. While for the convective, there's an adiabat with both boundary layers. For each convective case, the thickness of the thermal lid was computed with the methods described in the previous chapter. From this, we observe how the thermal lid is becoming thinner as the Ra increases described in Table 4.1

Ra/CMB	0.5R	0.6R	0.7R	0.8R	0.9R
1e5	593 km	471 km	536 km	174 km	92km
1e6	281 km	244 km	203 km	113 km	58km
1e7	187 km	122 km	142 km	72 km	28km

Table 4.1: Thermal lid thicknesses computed for all the parameter space.

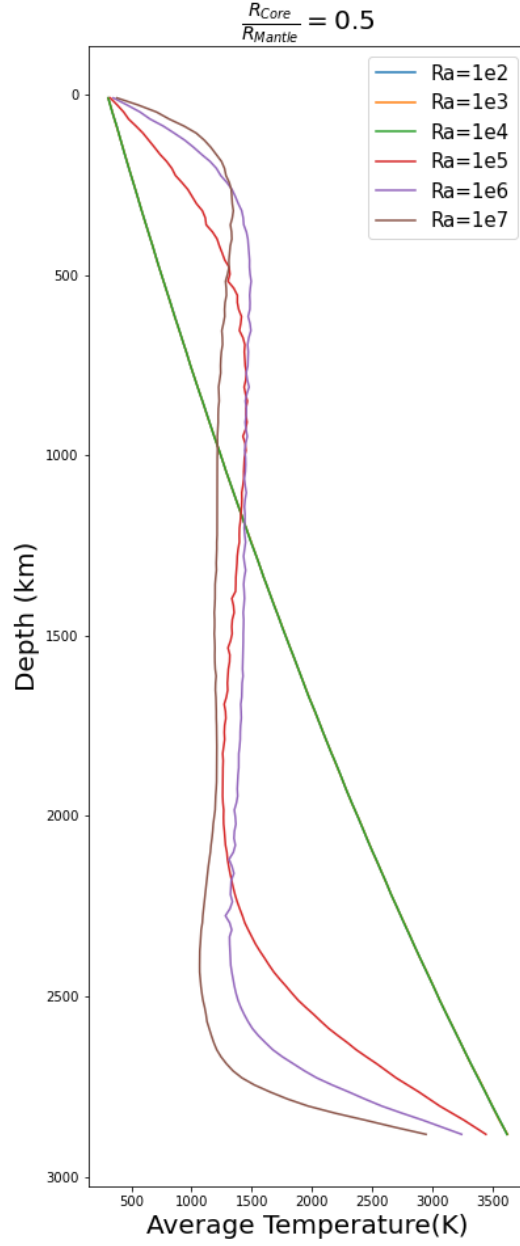


Figure 4.1: Temperature profiles for a CMB configuration $0.5R$ and different Ra . In this plot, only adiabatic heating was considered as a result of the compression of the rock by the weight of the overlying material. Thermal profiles between $10^2 < Ra < 10^4$ show the same conductive behavior, and then slow convection evolves as Ra increases.

4.1.1 Onset of convection

To characterize the dynamical regime for the explored configurations in terms of CMB and Ra, we mapped and classified them as conductive vs convective cases. I discuss here the general patterns for the two cases. Figure 4.2 shows what a nominal simulation in a conductive region looks like.

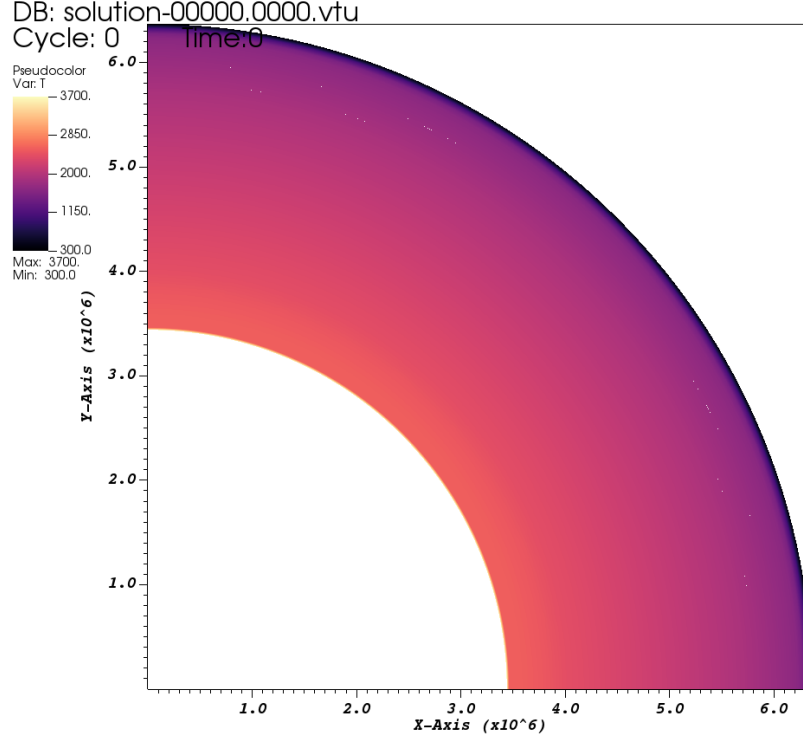


Figure 4.2: Snapshot of a simulation of a planet with CMB configuration 0.5R and $Ra=10^2$, The surface temperature is the same for all simulations $T=300K$ and the inner edge temperature is set according to the 1-D profiles, depending on the case of core-size.

Conversely, convective regimes show how hot plumes are rising from the CMB into a colder layer at the top, producing colder plumes sink into an inverse direction, which means starting from the top (Figure 4.3).

Nevertheless, these colder plumes cannot reach the CMB, their motion is impeded about halfway through the mantle once they're in contact with the material with the same T as the hot rising plumes. This will happen until the simulation reaches a temperature where the convection lets the system arrive at a constant temperature profile. At the same time, larger mantles can describe up to three major plumes evolving and mixing material in the quarter of annulus we are studying.

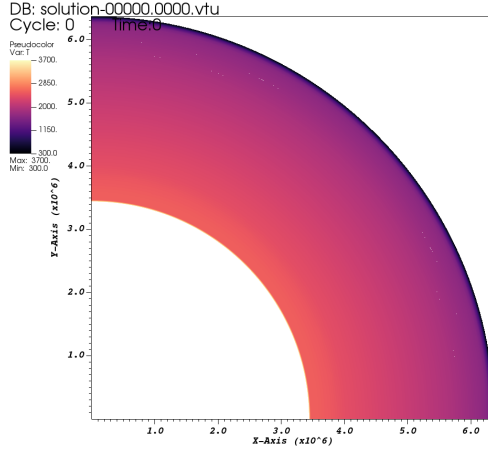
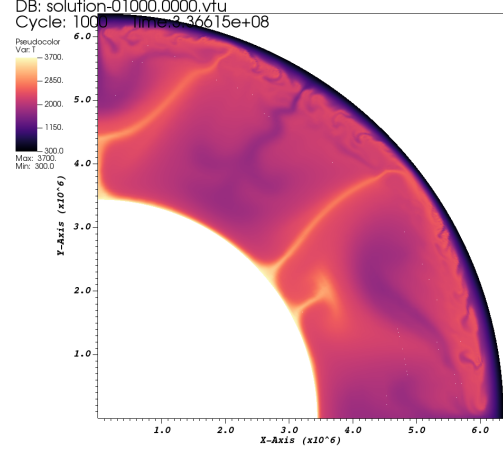
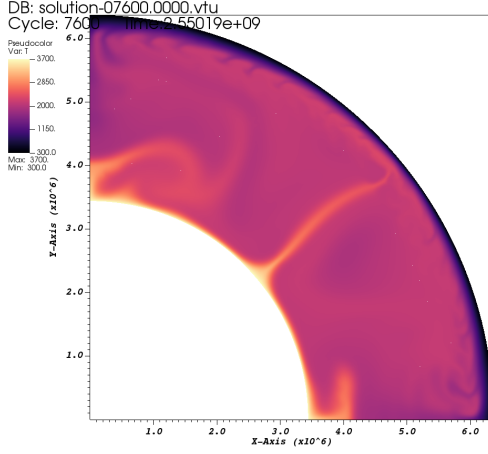
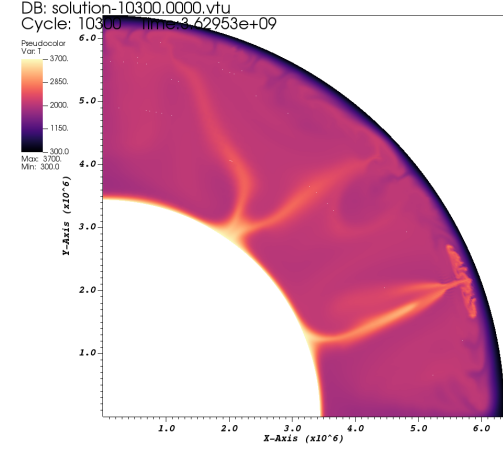
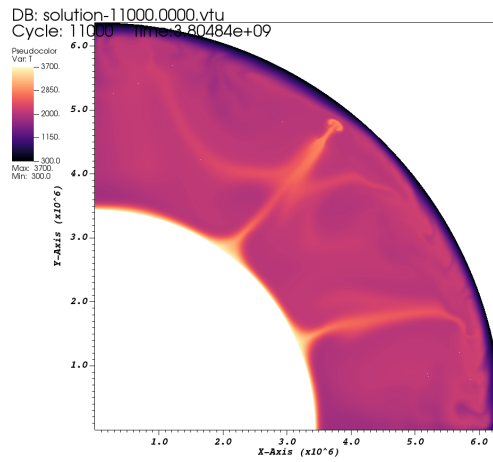
(a) Simulation at $t=0$ (b) Simulation at $t=3.3e8$ (c) Simulation at $t=2.5e9$ (d) Simulation at $t=3.6e9$ (e) Simulation at $t=3.8e9$

Figure 4.3: Snapshots of different times during a simulation for an Earth-like exoplanet, with CMB configuration $0.5R$ and $Ra = 10^7$, surface temperature at $300K$ and CMB temperature $\approx 3700K$. Plumes start to rise from the bottom of the mantle at $t=1.5e8$

Now that we identified CMB configurations and which Ra favors convection, we can map the two different regimes in the parameter space displayed on Figure 4.4.

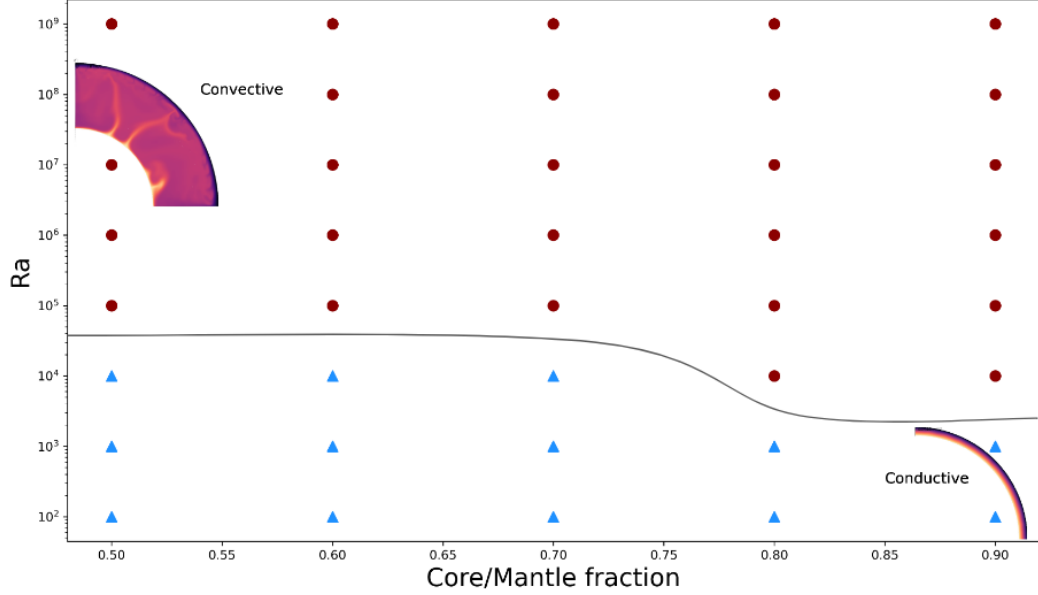


Figure 4.4: Parameter space described by the two heat transfer regimes, red dots represents all the simulations with thermal profiles and features that are characteristic of convection, and blue triangles represent the simulations that remain conductive after they reach the steady state of average temperature.

4.1.2 Melting production and water availability

In this work, a first-level approximation is made to determine under which ranges our studied configurations of mantles are convecting. From these simulations, we can compute the amount of water available following the parametrization relating the melting production to the associated amount of water available described in [Katz et al. \(2003\)](#) (See Section 2.2.3). This approach is valid for the first 300 km.

The results are shown in Figure 4.5 for the set of configurations in terms of Ra number and CMB radius. Where is it possible to identify the occurrence of melting for $\text{CMB} > 0.8R$. As mentioned before, as Ra increases, the thickness of the thermal lid reduces and, consequently, the intersection with the solidus temperature. In this way, for $\text{CMB} = 0.8R$, and consequently the presence of water. There's a maximum amount of melt produced at lower $\text{Ra} = 10^5$ (2.6×10^{-12} Earth's mass oceans). For higher Ra, the profile reduces the adiabatic mantle temperature moving away from the solidus temperature and reducing this area (See the Appendix section for all the profiles), showing a minimum at $\text{Ra} = 10^6$ of

5×10^{-13} Earth's mass oceans. Therefore, when $Ra=10^7$, the profile reduces the thickness of the lid, moving the curvature of the geotherm close to the surface and above the solidus and showing a higher melt value again. In the other case of $CMB=0.9R$, the amount of water delivered is linear, indicating that for more vigorous convection, melt production will be higher.

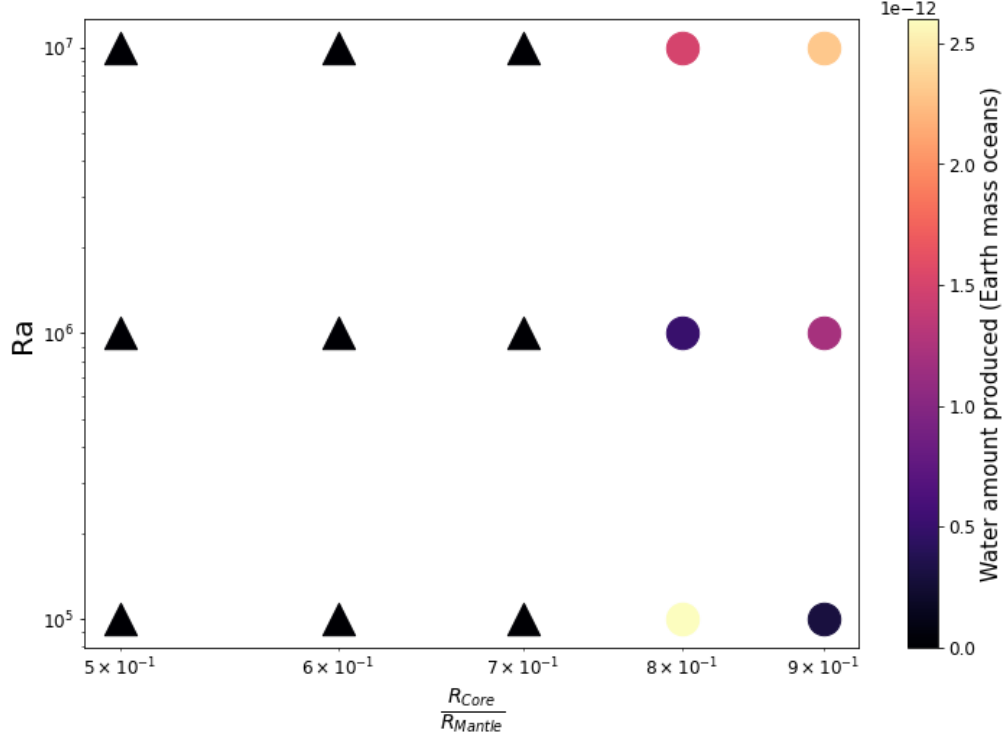


Figure 4.5: Convective regime described by different CMB configurations and Ra . Below $0.8R$, there's no presence of melt (triangles), not even including water. On the other side, for CMB configurations above $0.8R$ the optimal Ra to produce the higher amount of melt (circles) is $Ra=10^7$

4.1.3 Mobility regime

Following [Tackley \(2000\)](#), the mobility coefficient \mathbf{M} was computed for all the cases. This is, the ratio between the surface velocity (retrieved from the statistics post-processor of the velocity field) and the Root Mean Square (RMS) velocity of the mantle once it reaches stable convection. Figure 4.6 shows these results. For $CMB < 0.8R$ the mobility value is below 1, which means that the mantle convection is decoupled from the crust. Conversely, for $CMB=0.9R$, the values of all the Ra ranges are higher than 1, meaning that the surface velocity is high enough to interact dynamically with the mantle. This lets us map which CMB

and Ra are under the stagnant-lid regime and which are under the mobility-lid regime. It is necessary to highlight, that mobility doesn't mean directly the occurrence of plate tectonics. The latter is one result of these mechanisms but not the definitive one. The regime as the episodic lid is also part of the mobility regime, as they have episodes of the stagnant lid and mobile lid during time. It's interesting to note the higher mobility coefficients are the CMB configurations that show the presence of melt with volatiles on it, which means that in a real scenario, under these conditions, volcanism is possible. An eventual exchange between the interior and the atmosphere could be very efficient.

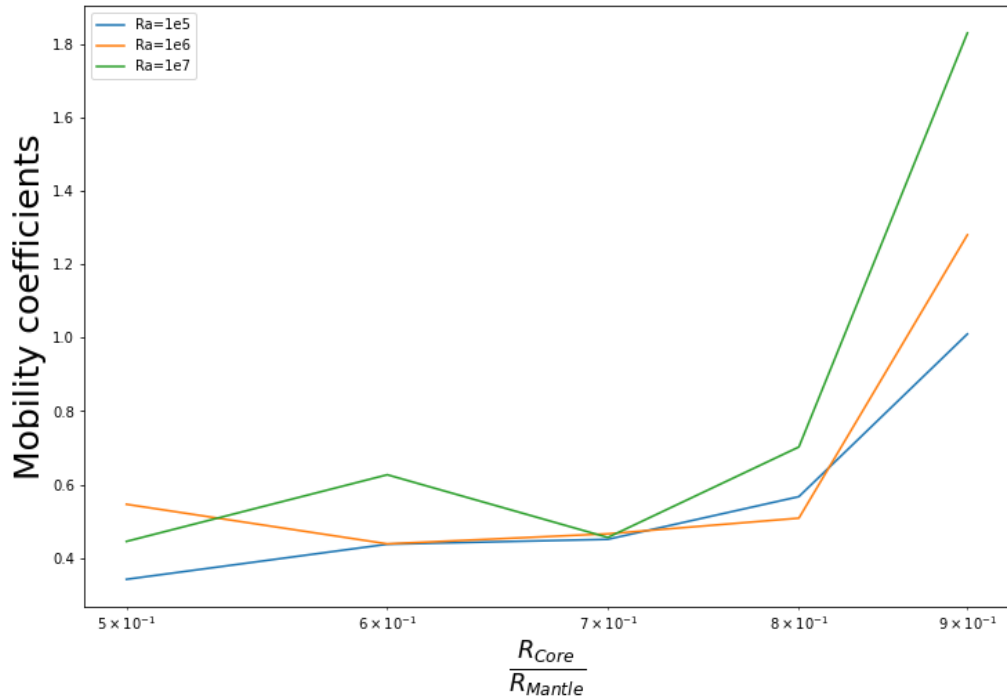


Figure 4.6: Mobility coefficients for different Ra numbers and core sizes following [Tackley \(2000\)](#). For values of $M \ll 1$ stagnant lid is assumed in the planet, meaning that the mantle is completely decoupled dynamically from the lid, with the latter becoming rigid and isolated in geological timescales. On the other side, for $M > 1$ the planet is under the regime of mobile-lid.

4.1.4 Impact of Heat sources

Finally, we explored the impact of the heat sources on our results (Figure 4.7). In this way, before computing the thermal profiles with all heat sources together, it was necessary to compute the individual contributions of each source to compare the evolution into a steady state of convergence. It clearly shows that for

$Ra=10^5$, there's a minimum distinction between shear and radiogenic heating. While Ra increases the difference between these two sources is remarkable, with shear heating contributing the most (312K higher than the radiogenic heat source profile).

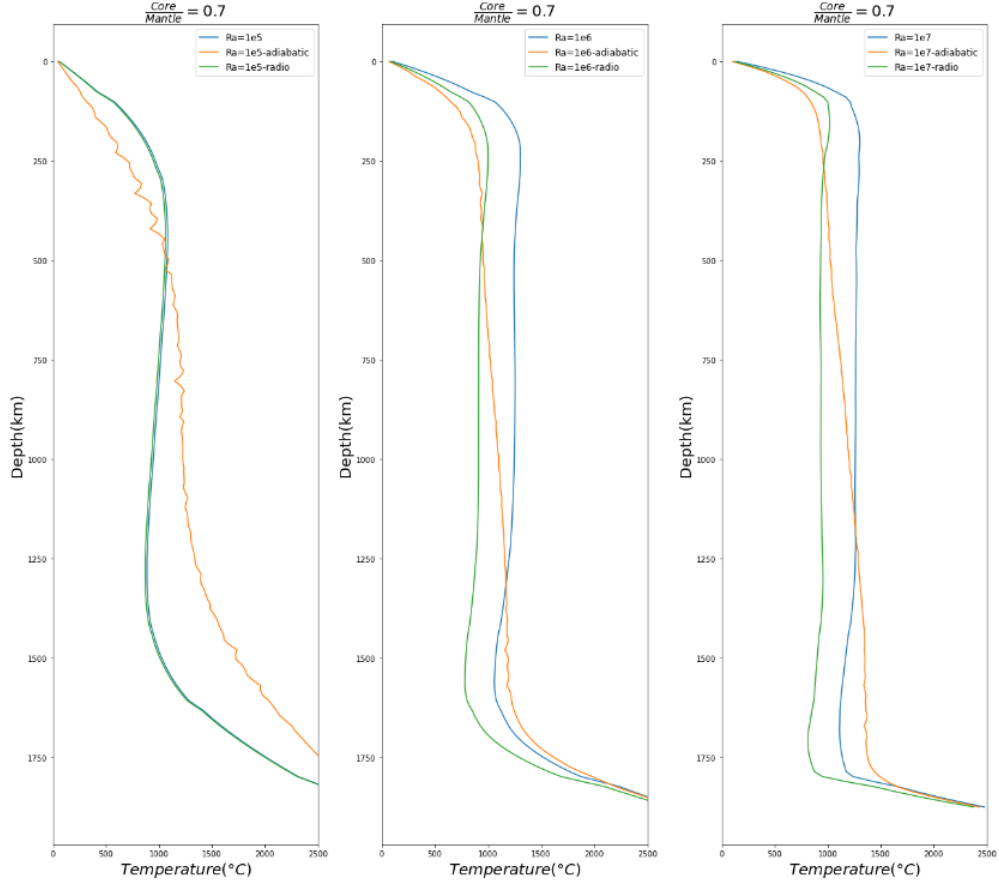


Figure 4.7: Thermal profiles for a CMB configuration 0.7R and different Ra numbers, for each Ra , three different heat sources were computed individually. Shear, adiabatic and radiogenic heating in blue, orange and green curves, respectively. In this case, as we are considering a homogeneous mantle, we didn't consider phase transitions and latent heat.

4.2 Internal structure of Trappist-1 planets

We examine the mass and radius of each TRAPPIST-1 planet based on the findings by [Agol et al. \(2021\)](#). While assuming a mantle composition similar to Earth, we only vary the core properties. Figure 4.8 illustrates the density profiles of all planets under the assumption of an Earth-like composition and a

surface temperature of 300 K. The figure showcases the internal structure and density profile of TRAPPIST-1b, considering different temperature assumptions and core size assumptions. Notably, the most significant discrepancies arise from the varying core sizes. In particular, when the core is smaller, the mantle exhibits a broader range of viscosity.

Furthermore, the presence of a larger core tends to result in a generally lower average viscosity compared to a smaller core, consequently affecting the dissipation outcomes. Moreover, the temperature increase also contributes to this effect by substantially reducing the mantle's viscosity by more than ten times. In this study, the heat profiles for all the Trappist-1 planets were computed for Bolmont et al. (in prep).

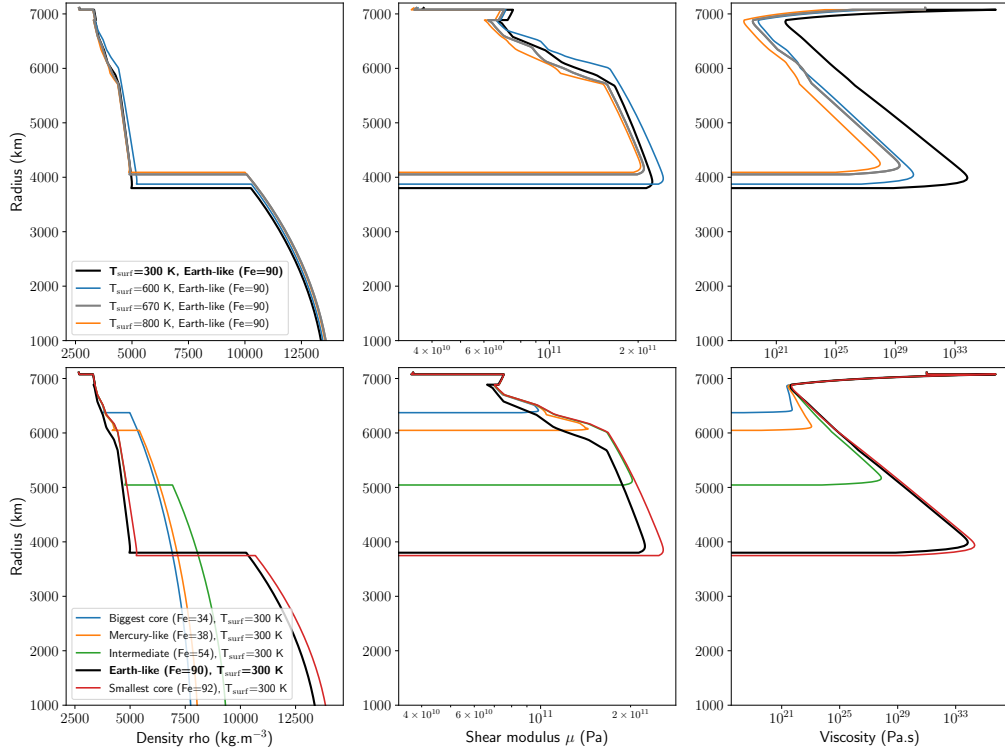


Figure 4.8: Density, shear modulus, and viscosity profiles of TRAPPIST-1b computed with the BurnMan code for different compositions. The top panel shows the influence of the temperature on the profile. The bottom panel shows the influence of composition on the profile.

Discussion

We presented in the last section the overview of the results of the parameter study in Earth-like exoplanet mantle's convection simulations. Several assumptions were taken into account when setting each model. For instance, a homogeneous mantle from the CMB to the surface and a surface temperature of 300K for all the configurations were considered. The amount of iron in the core varied according to the size of the mantle. To maintain the same observed density of the Earth, the viscosity in all cases was the order of $10^{22} Pa \cdot s$ (Turcotte and Schubert, 2002). The heat sources considered when solving the conservation equations are radiogenic, adiabatic, and shear heating. For the heating rates of radiogenic elements, a function was implemented to simulate a region from the upper mantle to double the amount of U and Th as on Earth and then re-scale it volumetrically for each mantle size. As we don't have any clue of how's the distribution of radiogenic elements in exoplanets, I assumed that because of partial melting, the radiogenic elements were going to be mobilized into these regions following similar Earth distribution.

In this case, the first significant result comes from the 1-D models part: when varying the CMB and the content of Iron in the core to replicate Earth's density, it was not possible to find solutions of self-consistent profiles of pressure, temperature, and gravity for $\frac{R_{core}}{R_{mantle}} < 0.5$. This means that smaller core sizes are less probable following the same molar fraction of the pyrolite composition on Earth in a homogeneous mantle. It is necessary to remark that molar fractions of light elements in the core were maintained the same for all cases following the midpoints of Zhang et al. (2021).

Consequently, when introducing these adiabatic profiles into the 2-D simulations was possible to identify the corresponding $Ra_{critical}$ for raising gravitational instabilities and then the onset of convection. For instance, $\frac{R_{core}}{R_{mantle}} \leq 0.7$ have a $Ra_{critical} = 10^4$ while for $\frac{R_{core}}{R_{mantle}} > 0.7$ the convection starts at $Ra_{critical} = 10^3$, below those values the main heat transport is conduction. Because of this, the convergence time is extremely fast. Meaning that is easier to break the conductive behavior in smaller mantles. This makes sense as described by Turcotte and Schubert (2002) where for values below $Ra_{critical}$, the buoyancy forces are not

strong enough to overcome friction forces, which means that the viscosity is more favorable in this configuration.

As we increased the Ra through the gravity values, an adaptative grid was necessary to solve the conservation equations on convective regimes. As the Rayleigh-Taylor instabilities were becoming thinner and more chaotic, the simulations had to re-organize the size of each cell based on temperature changes computed on the previous time step. In this way, we only performed simulations between $10^2 < Ra < 10^7$, as the higher the Ra , the structures were thinner and required more mesh refinement and consequently more computational time in agreement with [Bangerth et al. \(2022a\)](#). Furthermore, for the scope of this study, we choose to set the maximum Ra , as the estimates show for the lower Earth's mantle.

In this way, once the simulations converged, the next step was to compute the thermal lid thickness for each convective case. Identifying how increasing the Ra for each configuration led to a smaller lid, as expected from the adiabatic profile part of the theory section. It was also possible to observe, how high Ra showed colder profiles. Considering that the Ra number is a non-dimensional number that quantifies the convection vigor in a system, then for higher Ra , the convection is vigorous enough to let an efficient mixing and cooling of the thermal profile as described by [Ballmer and Noack \(2021\)](#). Nevertheless, I computed the different simulations just taking into account one heat source at a time, and all of them together to study the individual contribution of each term in the energy conservation equations, finding that radiogenic heating and shear heating have similar contributions for $Ra \leq 10^5$, and above that Ra , shear heating becomes much more important, which is physically correct, as the convection is more vigorous, resulting in higher kinetic energy that eventually will be transformed into heat as described by [Bangerth et al. \(2022b\)](#).

The volumetric amount of melt was computed and, consequently, the volumetric amount of water possible to deliver into the atmosphere. In these calculations, we assumed that all the water in the melt is outgassed by any means. When applying the parametrization of [Katz et al. \(2003\)](#) to compute the produced melt and the associated amount of available water based on the temperatures profiles output with our thermal evolution simulation, I found that only planet with $\frac{R_{core}}{R_{mantle}} \geq 0.8$ showed the presence of melt in the upper mantle (first 10GPa). All the amounts of water computed were around 10^9 kg, which is very low compared with the values of Earth's oceans (10^{21} kg). These results, bring us to the discussion of feedback between the interior and the atmosphere of rocky planets. In this case, a higher presence of melt near the surface can imply a higher probability of outgassing a thicker secondary atmosphere. Moreover, more volcanism will be a way to release heat more efficiently, making the process faster and letting the mantle cool down enough to make convection unsustainable in shorter timescales without the presence of plate tectonics.

Also, it is important to highlight, that the depth at which melt is produced differs according to the Ra , being closest to the surface for higher Ra . And this brings us to the last part of the project: investigating the surface regime of each configuration at different Ra . After computing the mobility coefficients for each case, it was possible to observe how all the planets with $\frac{R_{core}}{R_{mantle}} < 0.9$, $M \ll 1$, implying they are in a stagnant-lid configuration. This means that due to the strong convection in the mantle, the lid will experience very low stresses, and the bottom of the layer becomes completely decoupled, remaining in a dynamically isolated external crust (Ballmer and Noack, 2021). Conversely, a high mobility contrast was found for the configuration corresponding to the smallest mantle size. Implies that higher stresses act on the lid due to the upwellings and downwellings, localizing the deformation and opening the possibility of forming separate plates (Van Heck and Tackley, 2008). In this way, the configurations with bigger core sizes are the ones that show the presence of melt and high mobility coefficients. As a first-order approximation, this puts these internal structure configurations as the optimal candidates to release volatiles in some way to the atmosphere and then to have the ideal scenario in terms of stresses under the regime of the mobile lid dynamics.

Several studies have implemented diverse approximations for the **likelihood** of plate tectonics in exoplanets. Most are based on the viscosity profiles and the stresses present according to every model (e.g. Noack and Breuer (2014); Tackley (2000); Stamenković and Seager (2016)). From this, the viscosity is a property that depends on the heating rates or heating modes of exoplanets. This way, further studies must be done on the planet's formation stage, where radioactive elements are collected during accretion. To investigate the heating transport mechanisms as a result of different bulk compositions.

Conclusions

In this work, I explored the influence of the internal structure, from small to large mantle compared to the core, for Earth-sized exoplanets on the planetary geodynamical regime. For that purpose, I modeled different mantle sizes following the Earth's mantle composition. By simulating the heat transfer for various configurations in terms of mantle size and vigor of convection, we showed that for small mantle sizes, the heat sources considered in this study are enough to produce melt with the presence of water and show to be under the regime of mobile-lid, while for the rest of the mantle's configurations, a stagnant-lid regime was more likely. Being the small mantles case, the **optimal candidates** produce more volcanism and eventually release all the volatile content to replenish the corresponding atmosphere.

From this point, there are still many unanswered questions that can be the outlook of this project. For instance, applying these simulations with different surface temperatures to investigate the effect on the thickness of the thermal lid and consequently the respective stresses at the bottom of the layer. In order to identify if they can surpass the minimum threshold to break the basaltic crust and initiate and maintain subduction. At the same time, introduce the effect of heterogeneity within the mantle. Thus, the term corresponding to the latent heat would impact the thermal profile, moving the adiabat to the solidus temperature and resulting in a higher amount of melt and volatiles, respectively.

Moreover, another tool available from the simulations is the possibility of computing the geoid according to the convection cells' dynamic within the mantle, which can give us a first-order approach of the topography at the margins of each convective cell. Still, the **exogeodynamics** or study of exoplanets' geodynamical regime is a growing field of study. In that way, observational and modeling constraints can be done from the magma ocean stage to characterize the bulk composition and the heating link with the viscosity of the resulting mantle of exoplanets.

Bibliography

- E. Agol, C. Dorn, S. L. Grimm, M. Turbet, E. Ducrot, L. Delrez, M. Gillon, B.-O. Demory, A. Burdanov, K. Barkaoui, et al. Refining the transit-timing and photometric analysis of trappist-1: masses, radii, densities, dynamics, and ephemerides. *The planetary science journal*, 2(1):1, 2021.
- D. L. Anderson and A. M. Dziewonski. Upper mantle anisotropy: evidence from free oscillations. *Geophysical Journal International*, 69(2):383–404, 1982.
- M. D. Ballmer and L. Noack. The diversity of exoplanets: from interior dynamics to surface expressions. *Elements: An International Magazine of Mineralogy, Geochemistry, and Petrology*, 17(4):245–250, 2021.
- W. Bangerth, J. Dannberg, M. Fraters, R. Gassmoeller, A. Glerum, T. Heister, R. Myhill, and J. Naliboff. Aspect v2.4.0, July 2022a. URL <https://doi.org/10.5281/zenodo.6903424>.
- W. Bangerth, J. Dannberg, M. Fraters, R. Gassmoeller, A. Glerum, T. Heister, R. Myhill, and J. Naliboff. ASPECT: Advanced Solver for Problems in Earth’s ConvecTion, User Manual, July 2022b. URL <https://doi.org/10.6084/m9.figshare.4865333>. doi:10.6084/m9.figshare.4865333.
- A. C. Barr, V. Dobos, and L. L. Kiss. Interior structures and tidal heating in the trappist-1 planets. *Astronomy & Astrophysics*, 613:A37, 2018.
- E. Bolmont, S. N. Breton, G. Tobie, C. Dumoulin, S. Mathis, and O. Grasset. Solid tidal friction in multi-layer planets: application to earth, venus, a super earth and the trappist-1 planets-potential approximation of a multi-layer planet as a homogeneous body. *Astronomy & Astrophysics*, 644:A165, 2020.
- J. Connolly. The geodynamic equation of state: what and how. *Geochemistry, geophysics, geosystems*, 10(10), 2009.
- J. Connolly and K. Petrini. An automated strategy for calculation of phase diagram sections and retrieval of rock properties as a function of physical conditions. *Journal of Metamorphic Geology*, 20(7):697–708, 2002.
- J. A. Connolly. Computation of phase equilibria by linear programming: a tool for geodynamic modeling and its application to subduction zone decarbonation. *Earth and Planetary Science Letters*, 236(1-2):524–541, 2005.

- S. Cottaar, T. Heister, I. Rose, and C. Unterborn. Burnman: A lower mantle mineral physics toolkit. *Geochemistry, Geophysics, Geosystems*, 15(4):1164–1179, 2014.
- R. Dasgupta, M. M. Hirschmann, and N. D. Smith. Partial melting experiments of peridotite+ co₂ at 3 gpa and genesis of alkalic ocean island basalts. *Journal of Petrology*, 48(11):2093–2124, 2007.
- V. Dobos, A. C. Barr, and L. L. Kiss. Tidal heating and the habitability of the trappist-1 exoplanets. *Astronomy & Astrophysics*, 624:A2, 2019.
- C. Dorn, A. Khan, K. Heng, J. A. Connolly, Y. Alibert, W. Benz, and P. Tackley. Can we constrain the interior structure of rocky exoplanets from mass and radius measurements? *Astronomy & Astrophysics*, 577:A83, 2015.
- C. Dorn, J. Venturini, A. Khan, K. Heng, Y. Alibert, R. Helled, A. Rivoldini, and W. Benz. A generalized bayesian inference method for constraining the interiors of super earths and sub-neptunes. *Astronomy & Astrophysics*, 597:A37, 2017.
- P. Driscoll and D. Bercovici. Divergent evolution of earth and venus: influence of degassing, tectonics, and magnetic fields. *Icarus*, 226(2):1447–1464, 2013.
- E. Ducrot, M. Sestovic, B. Morris, M. Gillon, A. Triaud, J. De Wit, D. Thimmayappa, E. Agol, Y. Almleaky, A. Burdanov, et al. The 0.8–4.5 μm broadband transmission spectra of trappist-1 planets. *The Astronomical Journal*, 156(5):218, 2018.
- A. M. Dziewonski and D. L. Anderson. Preliminary reference earth model. *Physics of the earth and planetary interiors*, 25(4):297–356, 1981.
- B. J. Foley and P. E. Driscoll. Whole planet coupling between climate, mantle, and core: Implications for rocky planet evolution. *Geochemistry, Geophysics, Geosystems*, 17(5):1885–1914, 2016.
- F. R. Fontaine, G. Barruol, H. Tkalčić, I. Wölbern, G. Rümpler, T. Bodin, and M. Haugmard. Crustal and uppermost mantle structure variation beneath la réunion hotspot track. *Geophysical Journal International*, 203(1):107–126, 2015.
- E. A. Frank, B. S. Meyer, and S. J. Mojzsis. A radiogenic heating evolution model for cosmochemically earth-like exoplanets. *Icarus*, 243:274–286, 2014.
- M. Gillon, A. H. Triaud, B.-O. Demory, E. Jehin, E. Agol, K. M. Deck, S. M. Lederer, J. De Wit, A. Burdanov, J. G. Ingalls, et al. Seven temperate terrestrial planets around the nearby ultracool dwarf star trappist-1. *Nature*, 542(7642):456–460, 2017.

- O. Grasset, J. Schneider, and C. Sotin. A study of the accuracy of mass–radius relationships for silicate-rich and ice-rich planets up to 100 earth masses. *The Astrophysical Journal*, 693(1):722, 2009.
- S. L. Grimm, B.-O. Demory, M. Gillon, C. Dorn, E. Agol, A. Burdanov, L. Delrez, M. Sestovic, A. H. Triaud, M. Turbet, et al. The nature of the trappist-1 exoplanets. *Astronomy & Astrophysics*, 613:A68, 2018.
- J. Grotzinger and T. H. Jordan. *Understanding earth*. Macmillan, 2010.
- B. Harte and J. Harris. Lower mantle mineral associations preserved in diamonds. *Mineralogical Magazine*, 58(1):384–385, 1994.
- Y. He, E. G. Puckett, and M. I. Billen. A discontinuous Galerkin method with a bound preserving limiter for the advection of non-diffusive fields in solid earth geodynamics. *Physics of the Earth and Planetary Interiors*, 263: 23 – 37, 2017. ISSN 0031-9201. doi: 10.1016/j.pepi.2016.12.001. URL <https://doi.org/10.1016/j.pepi.2016.12.001>.
- T. Heister, J. Dannberg, R. Gassmüller, and W. Bangerth. High accuracy mantle convection simulation through modern numerical methods. II: Realistic models and problems. *Geophysical Journal International*, 210(2):833–851, 2017. doi: 10.1093/gji/ggx195. URL <https://doi.org/10.1093/gji/ggx195>.
- A. W. Hofmann. Mantle geochemistry: the message from oceanic volcanism. *Nature*, 385(6613):219–229, 1997.
- A. R. Howe, A. Burrows, and W. Verne. Mass-radius relations and core-envelope decompositions of super-earths and sub-neptunes. *The Astrophysical Journal*, 787(2):173, 2014.
- J. M. Jenkins, D. A. Caldwell, H. Chandrasekaran, J. D. Twicken, S. T. Bryson, E. V. Quintana, B. D. Clarke, J. Li, C. Allen, P. Tenenbaum, et al. Overview of the kepler science processing pipeline. *The Astrophysical Journal Letters*, 713(2):L87, 2010.
- S.-i. Karato and S. Barbot. Dynamics of fault motion and the origin of contrasting tectonic style between earth and venus. *Scientific Reports*, 8(1):1–11, 2018.
- J. F. Kasting, D. P. Whitmire, and R. T. Reynolds. Habitable zones around main sequence stars. *Icarus*, 101(1):108–128, 1993.
- R. F. Katz, M. Spiegelman, and C. H. Langmuir. A new parameterization of hydrous mantle melting. *Geochemistry, Geophysics, Geosystems*, 4(9), 2003.
- S. Kesson, J. Fitz Gerald, and J. Shelley. Mineral chemistry and density of subducted basaltic crust at lower-mantle pressures. *Nature*, 372(6508):767–769, 1994.

D. G. Koch, W. J. Borucki, G. Basri, N. M. Batalha, T. M. Brown, D. Caldwell, J. Christensen-Dalsgaard, W. D. Cochran, E. DeVore, E. W. Dunham, et al. Kepler mission design, realized photometric performance, and early science. *The Astrophysical Journal Letters*, 713(2):L79, 2010.

M. Kronbichler, T. Heister, and W. Bangerth. High accuracy mantle convection simulation through modern numerical methods. *Geophysical Journal International*, 191:12–29, 2012. doi: 10.1111/j.1365-246X.2012.05609.x. URL <http://dx.doi.org/10.1111/j.1365-246X.2012.05609.x>.

A. Lenardic. Volcanic-tectonic modes and planetary life potential. *Handbook of exoplanets*, pages 2897–2916, 2018.

T. Lichtenberg, L. K. Schaefer, M. Nakajima, and R. A. Fischer. Geophysical evolution during rocky planet formation. *arXiv preprint arXiv:2203.10023*, 2022.

D. L. Lourenço, A. Rozel, and P. J. Tackley. Melting-induced crustal production helps plate tectonics on earth-like planets. *Earth and Planetary Science Letters*, 439:18–28, 2016.

R. Luger, M. Sestovic, E. Kruse, S. L. Grimm, B.-O. Demory, E. Agol, E. Bolmont, D. Fabrycky, C. S. Fernandes, V. Van Grootel, et al. A seven-planet resonant chain in trappist-1. *Nature Astronomy*, 1(6):0129, 2017.

S. Maruyama, M. Ikoma, H. Genda, K. Hirose, T. Yokoyama, and M. Santosh. The naked planet earth: most essential pre-requisite for the origin and evolution of life. *Geoscience Frontiers*, 4(2):141–165, 2013.

M. Mayor and D. Queloz. A jupiter-mass companion to a solar-type star. *nature*, 378(6555):355–359, 1995.

W. F. McDonough and S.-S. Sun. The composition of the earth. *Chemical geology*, 120(3-4):223–253, 1995.

A. Mocquet, O. Grasset, and C. Sotin. Very high-density planets: a possible remnant of gas giants. *Philosophical Transactions of the Royal Society A: Mathematical, Physical and Engineering Sciences*, 372(2014):20130164, 2014.

R. O. Moore and J. J. Gurney. Pyroxene solid solution in garnets included in diamond. *Nature*, 318:553–555, 1985.

R. Myhill, S. Cottaar, T. Heister, I. Rose, and C. Unterborn. Burnman v1.1.0, Sept. 2022. URL <https://doi.org/10.5281/zenodo.7080174>.

L. Noack and D. Breuer. Plate tectonics on rocky exoplanets: influence of initial conditions and mantle rheology. *Planetary and Space Science*, 98:41–49, 2014.

- M. Ogawa. Numerical models of magmatism in convecting mantle with temperature-dependent viscosity and their implications for venus and earth. *Journal of Geophysical Research: Planets*, 105(E3):6997–7012, 2000.
- M. Ogawa and T. Yanagisawa. Mantle evolution in venus due to magmatism and phase transitions: From punctuated layered convection to whole-mantle convection. *Journal of Geophysical Research: Planets*, 119(4):867–883, 2014.
- J. O’Neil, H. Rizo, M. Boyet, R. Carlson, and M. Rosing. Geochemistry and isotopic characteristics of earth’s hadean mantle and primitive crust. *Earth and Planetary Science Letters*, 442:194–205, 2016.
- J. Otegi, F. Bouchy, and R. Helled. Revisited mass-radius relations for exoplanets below 120 m. *Astronomy & Astrophysics*, 634:A43, 2020a.
- J. F. Otegi, C. Dorn, R. Helled, F. Bouchy, J. Haldemann, and Y. Alibert. Impact of the measured parameters of exoplanets on the inferred internal structure. *Astronomy & Astrophysics*, 640:A135, 2020b.
- A. Ringwood. Role of the transition zone and 660 km discontinuity in mantle dynamics. *Physics of the Earth and Planetary Interiors*, 86(1-3):5–24, 1994.
- A. E. Ringwood. Phase transformations and their bearing on the constitution and dynamics of the mantle. *Geochimica et Cosmochimica Acta*, 55(8):2083–2110, 1991.
- L. Rogers and S. Seager. Three possible origins for the gas layer on gj 1214b. *The Astrophysical Journal*, 716(2):1208, 2010.
- T. Rolf, M. Weller, A. Gülcher, P. Byrne, J. G. O’Rourke, R. Herrick, E. Bjornnes, A. Davaille, R. Ghail, C. Gillmann, et al. Dynamics and evolution of venus’ mantle through time. *Space Science Reviews*, 218(8):70, 2022.
- I. Rose, B. Buffett, and T. Heister. Stability and accuracy of free surface time integration in viscous flows. *Physics of the Earth and Planetary Interiors*, 262:90 – 100, 2017. ISSN 0031-9201. doi: 10.1016/j.pepi.2016.11.007. URL <http://dx.doi.org/10.1016/j.pepi.2016.11.007>.
- V. Sautter, S. E. Haggerty, and S. Field. Ultradeep (> 300 kilometers) ultramafic xenoliths: Petrological evidence from the transition zone. *Science*, 252(5007):827–830, 1991.
- S. Seager, M. Kuchner, C. Hier-Majumder, and B. Militzer. Mass-radius relationships for solid exoplanets. *The Astrophysical Journal*, 669(2):1279, 2007.
- B. S. Smith, R. Danchin, J. Harris, and K. Stracke. Kimberlites near orroroo, south australia. In *Developments in Petrology*, volume 11, pages 121–142. Elsevier, 1984.

- V. Solomatov and L.-N. Moresi. Stagnant lid convection on venus. *Journal of Geophysical Research: Planets*, 101(E2):4737–4753, 1996.
- C. Sotin, O. Grasset, and A. Mocquet. Mass–radius curve for extrasolar earth-like planets and ocean planets. *Icarus*, 191(1):337–351, 2007.
- V. Stamenković and S. Seager. Emerging possibilities and insuperable limitations of exogeophysics: The example of plate tectonics. *The Astrophysical Journal*, 825(1):78, 2016.
- L. Stixrude. Talc under tension and compression: Spinodal instability, elasticity, and structure. *Journal of Geophysical Research: Solid Earth*, 107(B12): ECV–2, 2002.
- L. Stixrude and C. Lithgow-Bertelloni. Thermodynamics of mantle minerals—i. physical properties. *Geophysical Journal International*, 162(2):610–632, 2005.
- B. Stracke, N. Tosi, M. Godolt, T. Ruedas Gomez, J. L. Grenfell, D. Höning, A. Nikolaou, A.-C. Plesa, D. Breuer, and T. Spohn. On the habitability of a stagnant-lid earth. 2016.
- P. J. Tackley. Mantle convection and plate tectonics: Toward an integrated physical and chemical theory. *Science*, 288(5473):2002–2007, 2000.
- M. Turbet, E. Bolmont, J. Leconte, F. Forget, F. Selsis, G. Tobie, A. Caldas, J. Naar, and M. Gillon. Modeling climate diversity, tidal dynamics and the fate of volatiles on trappist-1 planets. *Astronomy & Astrophysics*, 612:A86, 2018.
- D. L. Turcotte and G. Schubert. *Geodynamics*. Cambridge university press, 2002.
- D. Valencia, D. D. Sasselov, and R. J. O’Connell. Detailed models of super-earths: How well can we infer bulk properties? *The Astrophysical Journal*, 665(2):1413, 2007.
- H. Van Heck and P. Tackley. Planforms of self-consistently generated plates in 3d spherical geometry. *Geophysical Research Letters*, 35(19), 2008.
- P. D. Ward and D. Brownlee. *The life and death of planet Earth: how the new science of astrobiology charts the ultimate fate of our world*. Macmillan, 2003.
- D. J. Weidner and Y. Wang. Phase transformations: Implications for mantle structure. *Washington DC American Geophysical Union Geophysical Monograph Series*, 117:215–235, 2000.
- Z. Zhang, D.-B. Zhang, K. Onga, A. Hasegawa, K. Ohta, K. Hirose, and R. M. Wentzcovitch. Thermal conductivity of casio 3 perovskite at lower mantle conditions. *Physical Review B*, 104(18):184101, 2021.

APPENDIX A

Appendix

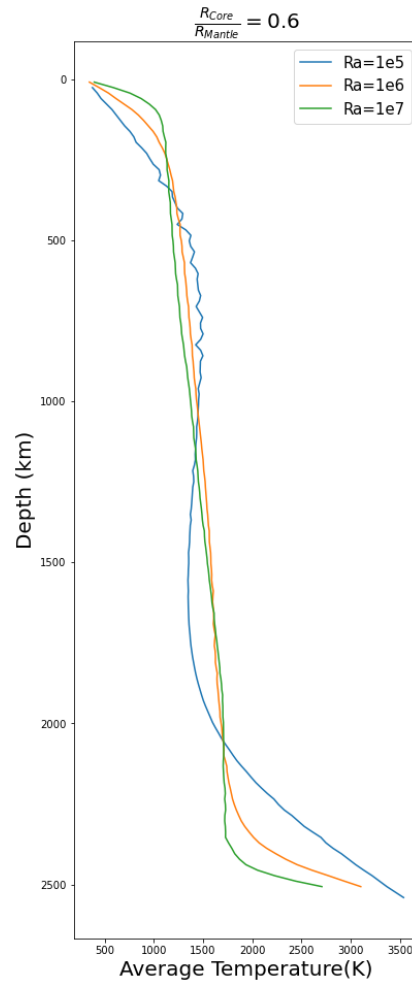


Figure A.1: Temperature profiles for a CMB configuration 0.6R and different Ra.

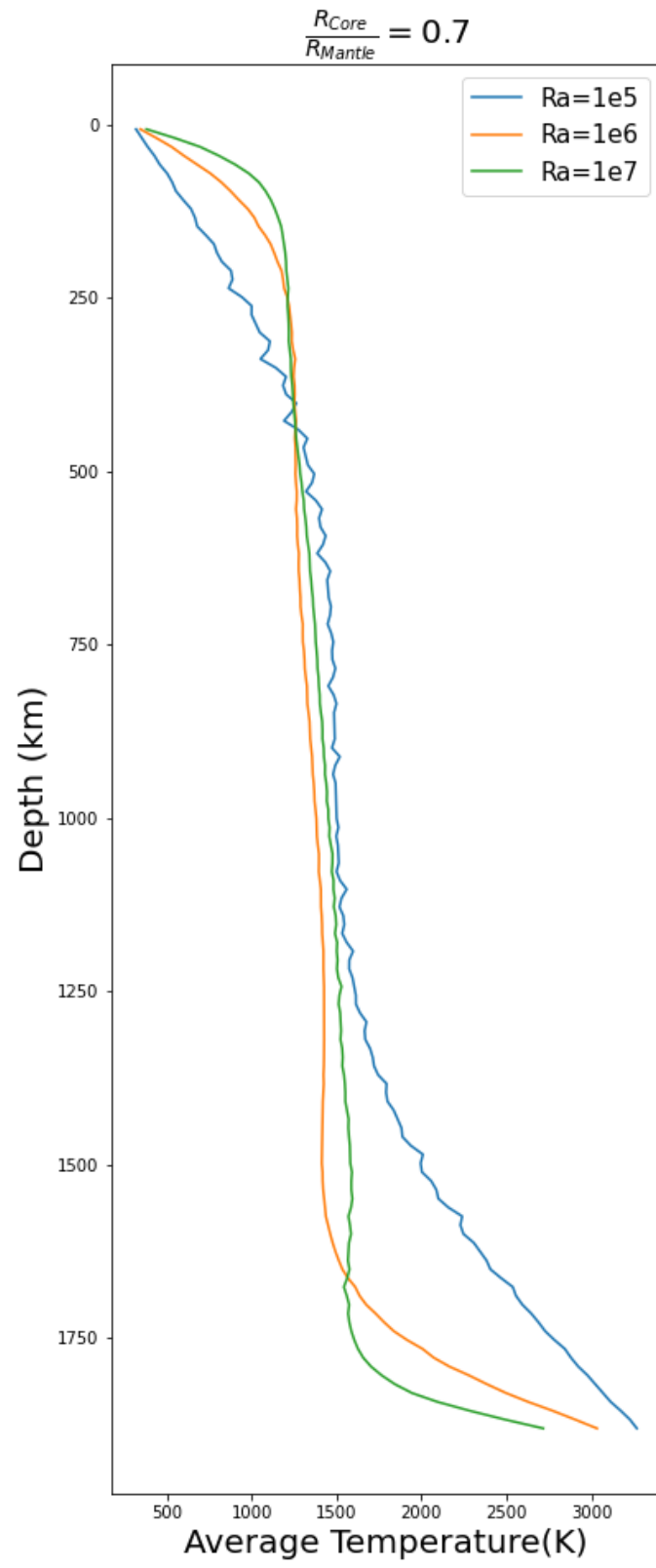


Figure A.2: Temperature profiles for a CMB configuration 0.7R and different Ra.

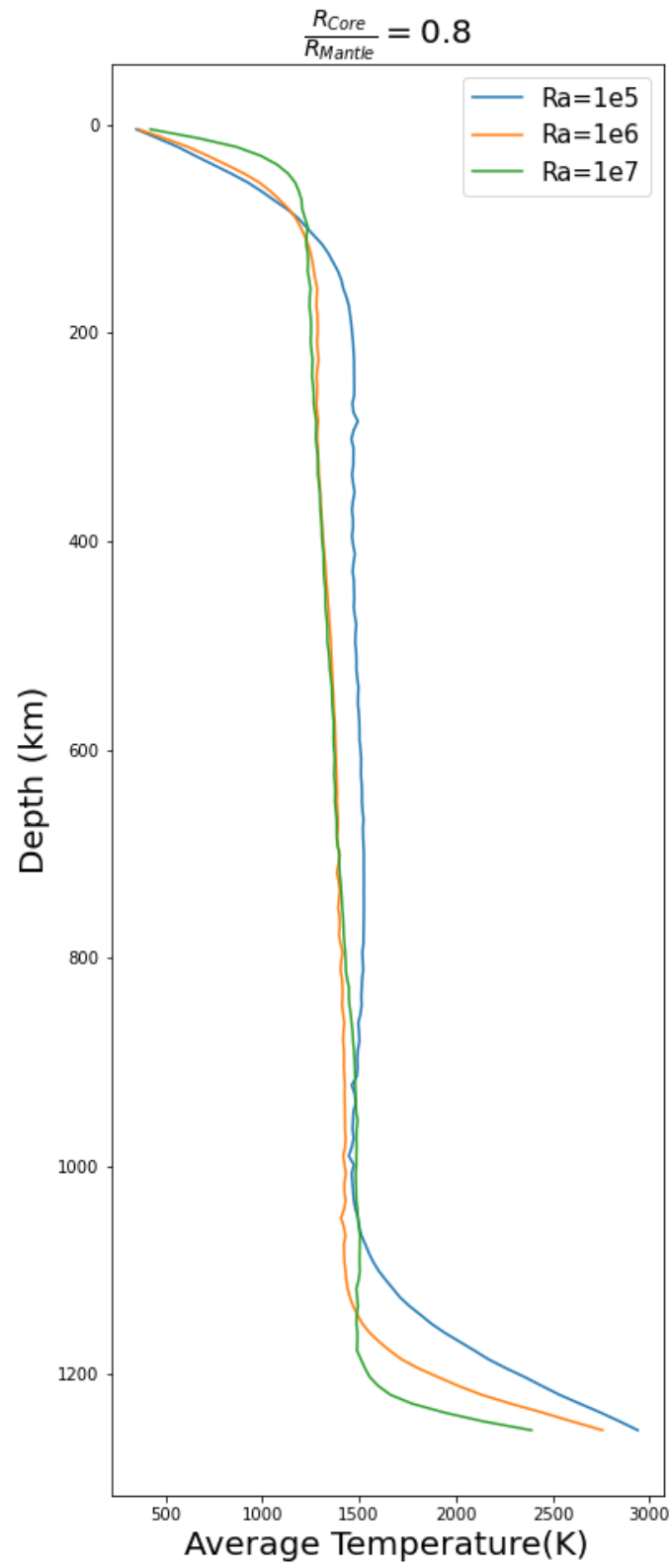


Figure A.3: Temperature profiles for a CMB configuration 0.8R and different Ra .

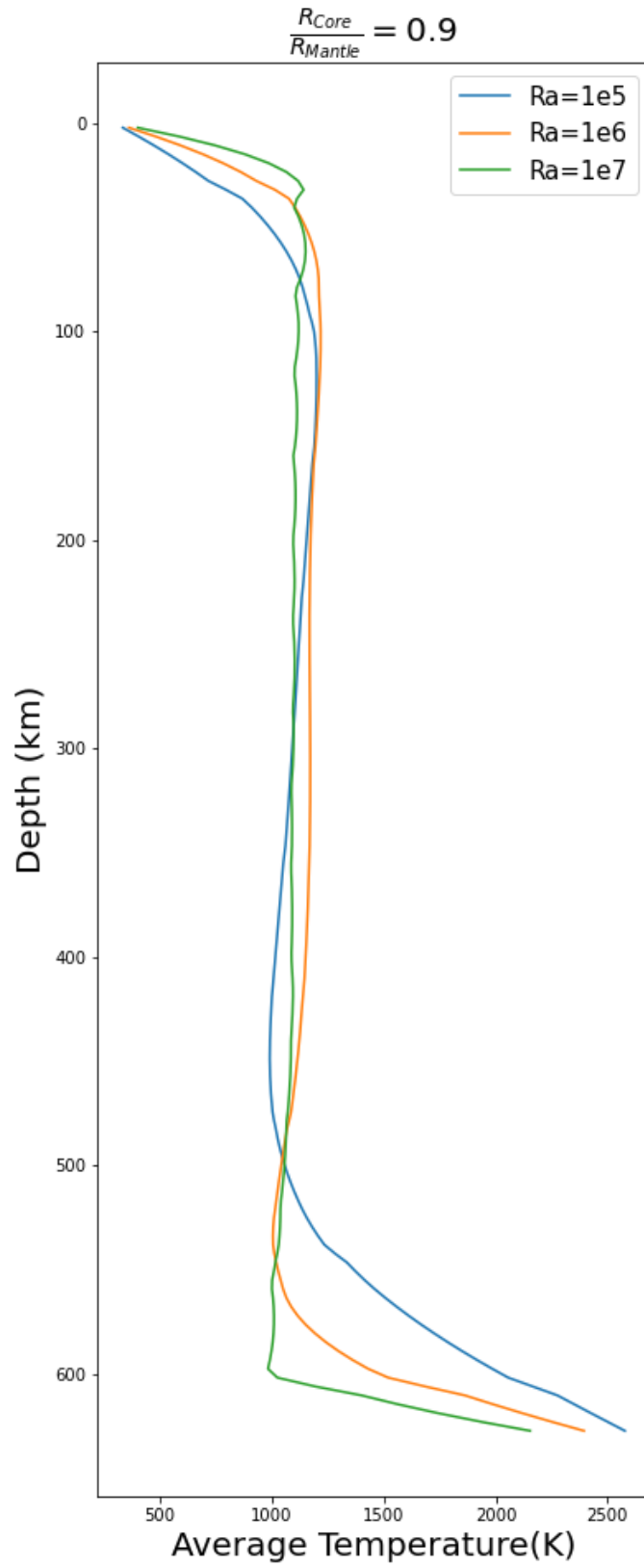


Figure A.4: Temperature profiles for a CMB configuration 0.9R and different Ra.

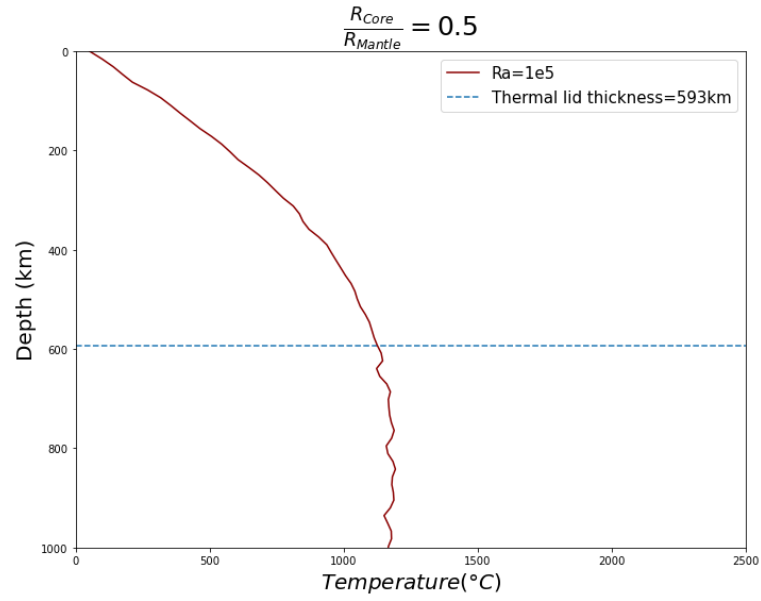


Figure A.5: Adiabatic profile for the first 300km in a CMB configuration 0.5R and $Ra = 1e5$, the thickness of the thermal lid is defined finding the second derivative of the adiabat.

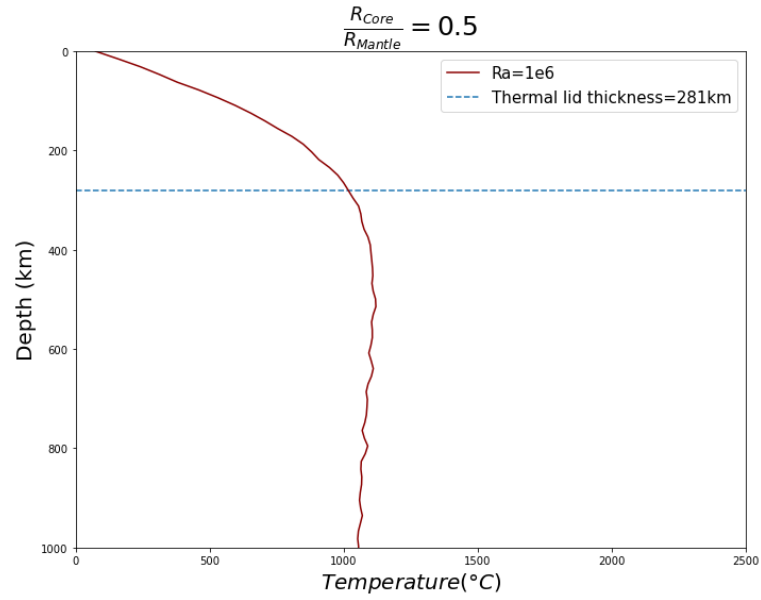


Figure A.6: Adiabatic profile for the first 300km in a CMB configuration 0.5R and $Ra = 1e6$, the thickness of the thermal lid is defined finding the second derivative of the adiabat.

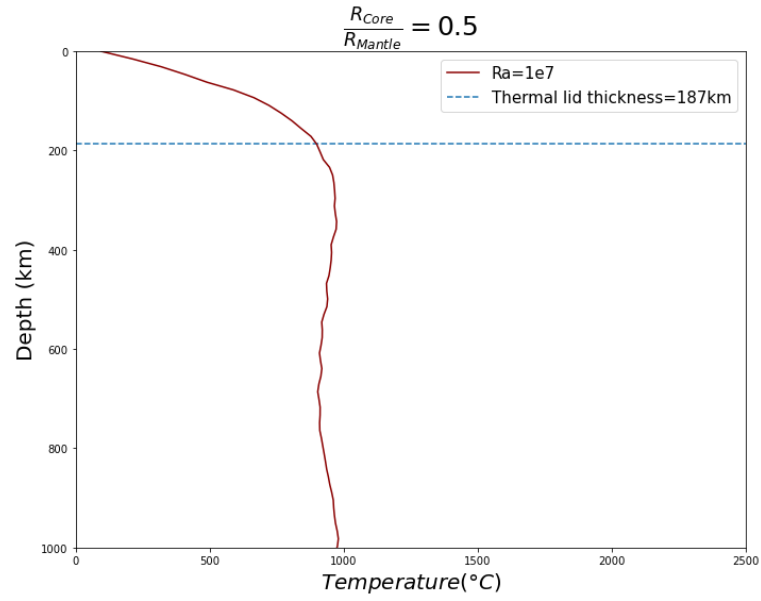


Figure A.7: Adiabatic profile for the first 300km in a CMB configuration 0.5R and $Ra=1e7$, the thickness of the thermal lid is defined finding the second derivative of the adiabat.

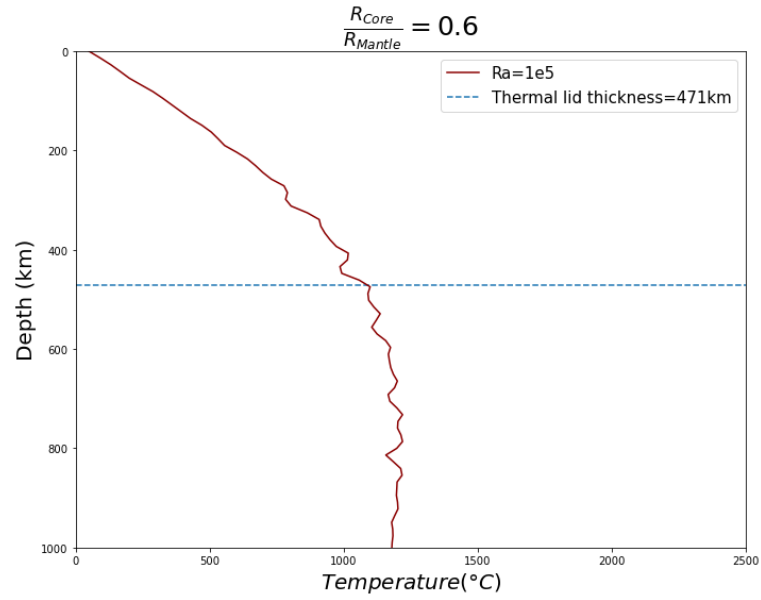


Figure A.8: Adiabatic profile for the first 300km in a CMB configuration 0.6R and $Ra=1e5$, the thickness of the thermal lid is defined finding the second derivative of the adiabat.

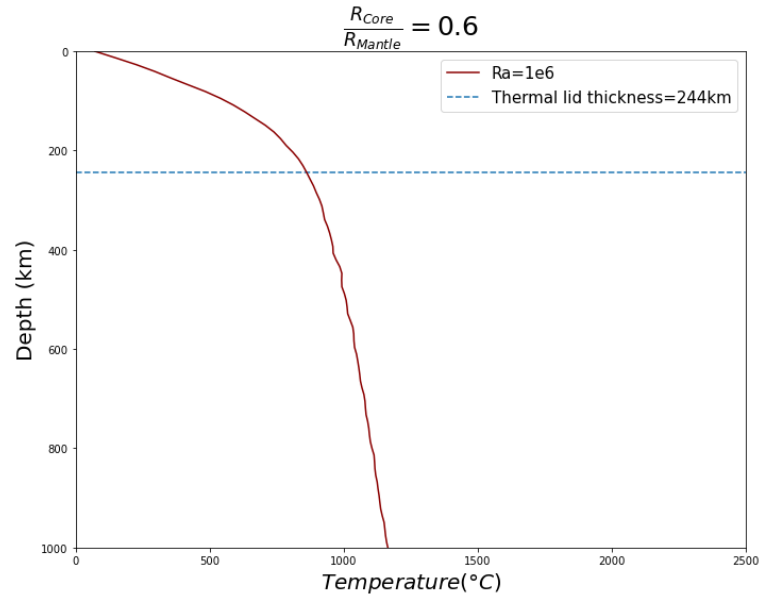


Figure A.9: Adiabatic profile for the first 300km in a CMB configuration 0.6R and $Ra=1e6$, the thickness of the thermal lid is defined finding the second derivative of the adiabat.

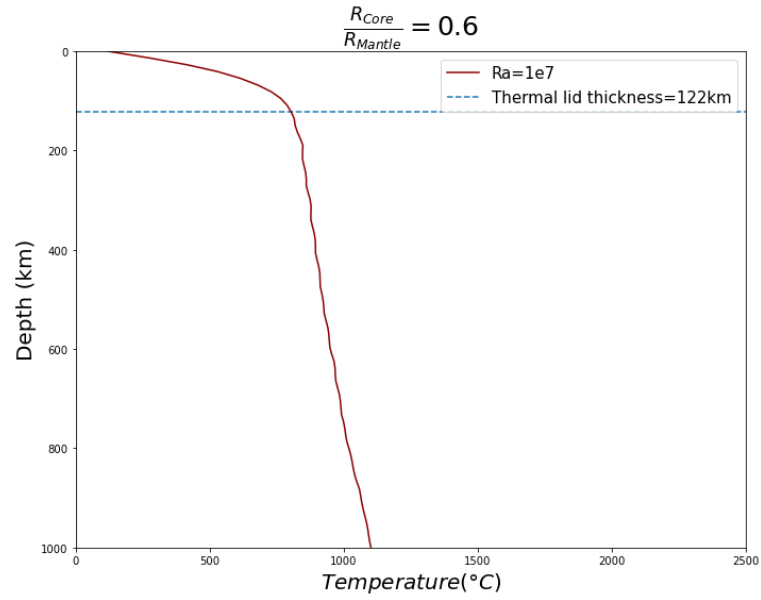


Figure A.10: Adiabatic profile for the first 300km in a CMB configuration 0.6R and $Ra=1e7$, the thickness of the thermal lid is defined finding the second derivative of the adiabat.

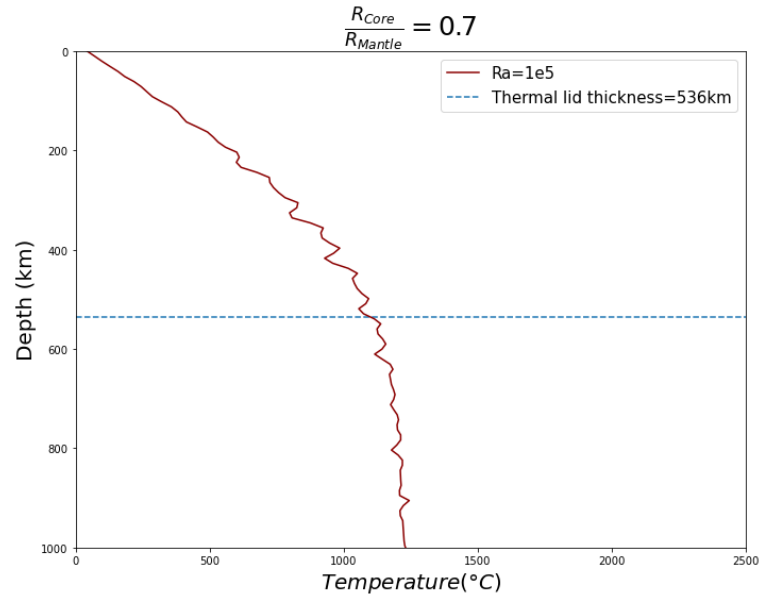


Figure A.11: Adiabatic profile for the first 300km in a CMB configuration 0.7R and $Ra = 1e5$, the thickness of the thermal lid is defined finding the second derivative of the adiabat.

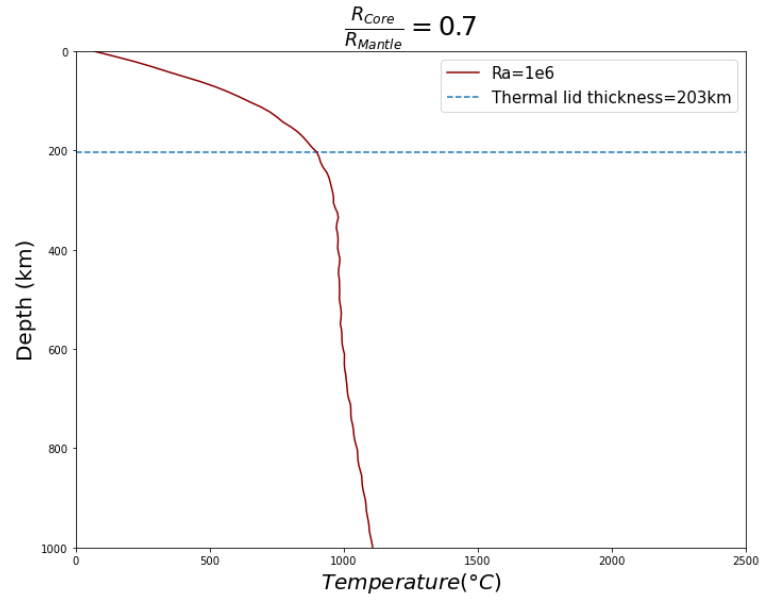


Figure A.12: Adiabatic profile for the first 300km in a CMB configuration 0.7R and $Ra = 1e6$, the thickness of the thermal lid is defined finding the second derivative of the adiabat.

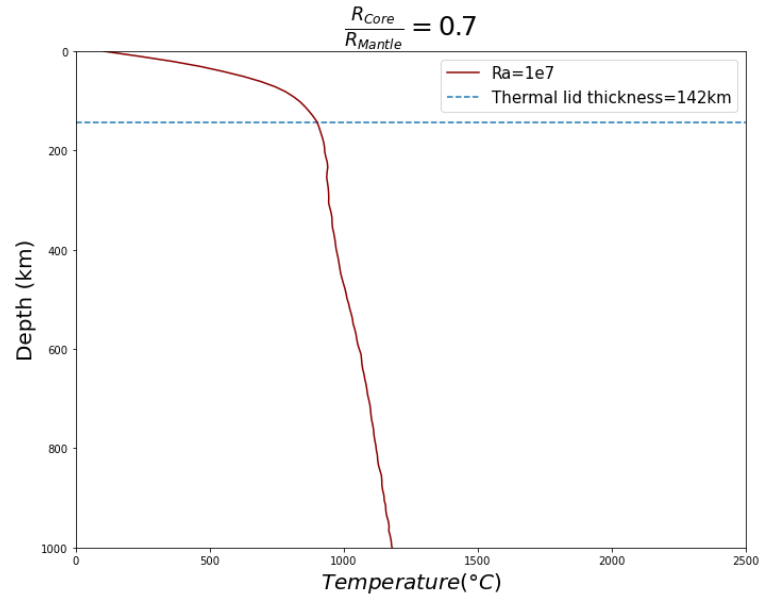


Figure A.13: Adiabatic profile for the first 300km in a CMB configuration 0.7R and $Ra=1e7$, the thickness of the thermal lid is defined finding the second derivative of the adiabat.

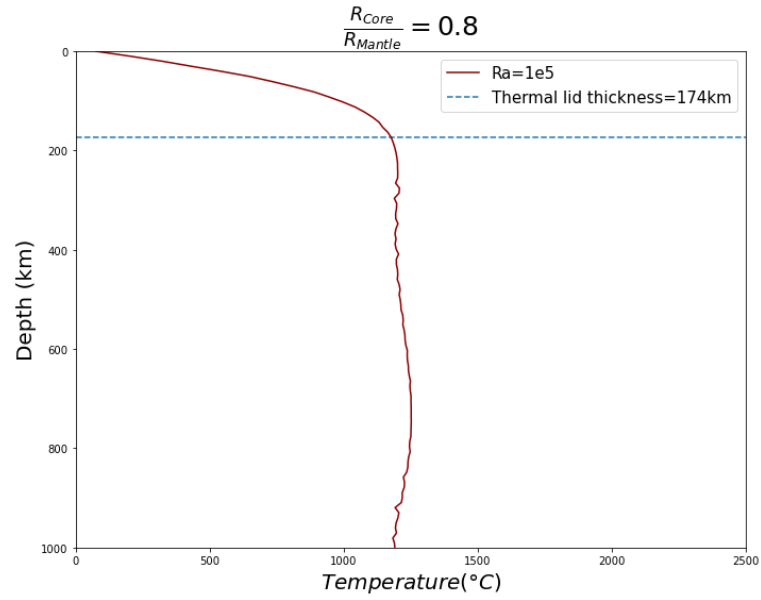


Figure A.14: Adiabatic profile for the first 300km in a CMB configuration 0.8R and $Ra=1e5$, the thickness of the thermal lid is defined finding the second derivative of the adiabat.

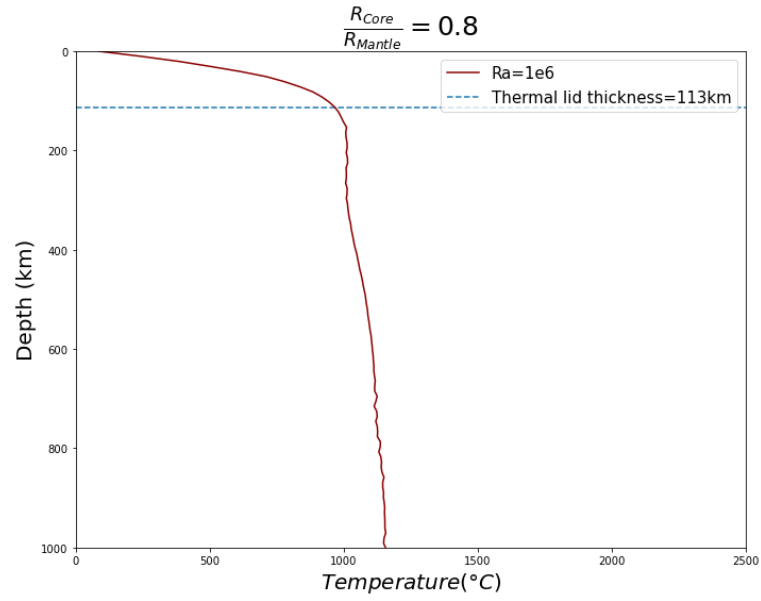


Figure A.15: Adiabatic profile for the first 300km in a CMB configuration 0.8R and $Ra=1e6$, the thickness of the thermal lid is defined finding the second derivative of the adiabat.

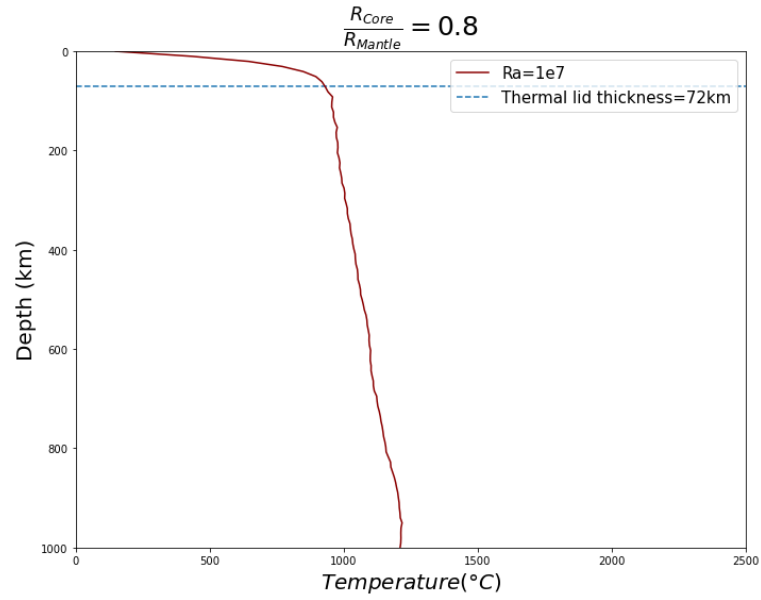


Figure A.16: Adiabatic profile for the first 300km in a CMB configuration 0.8R and $Ra=1e7$, the thickness of the thermal lid is defined finding the second derivative of the adiabat.

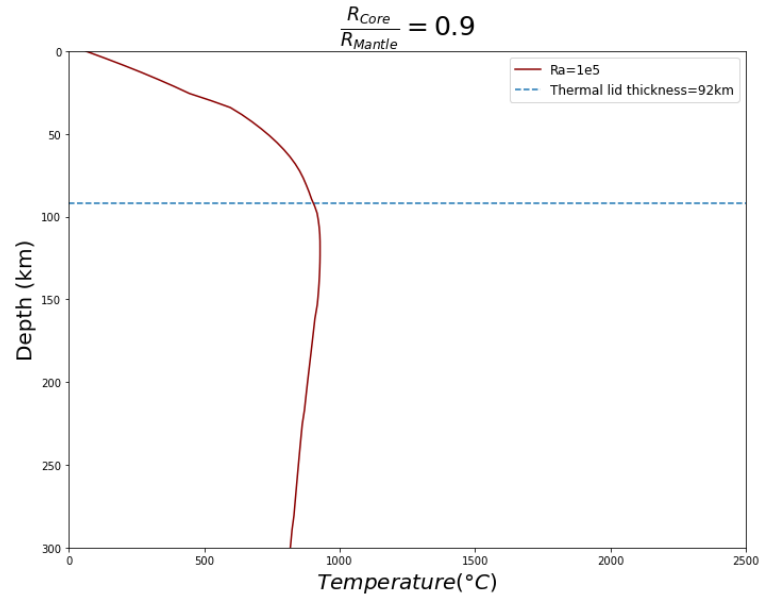


Figure A.17: Adiabatic profile for the first 300km in a CMB configuration 0.9R and $Ra=1e5$, the thickness of the thermal lid is defined finding the second derivative of the adiabat.

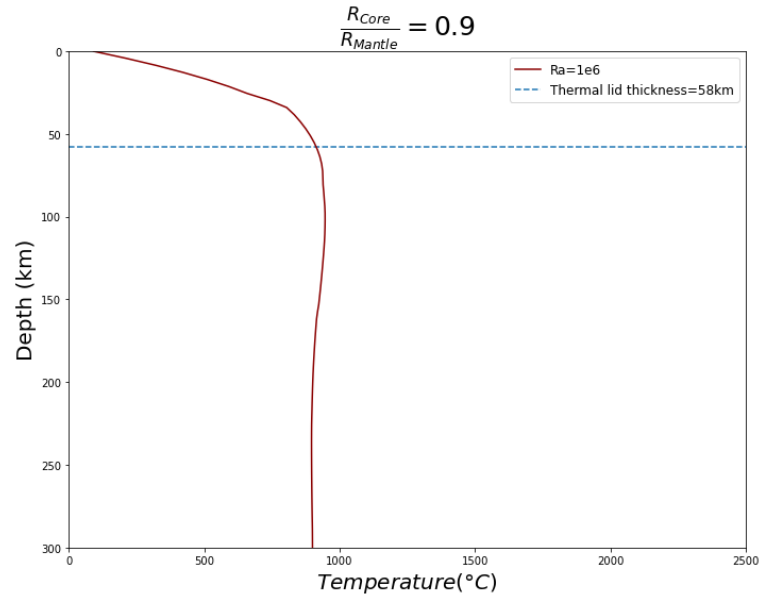


Figure A.18: Adiabatic profile for the first 300km in a CMB configuration 0.9R and $Ra=1e6$, the thickness of the thermal lid is defined finding the second derivative of the adiabat.

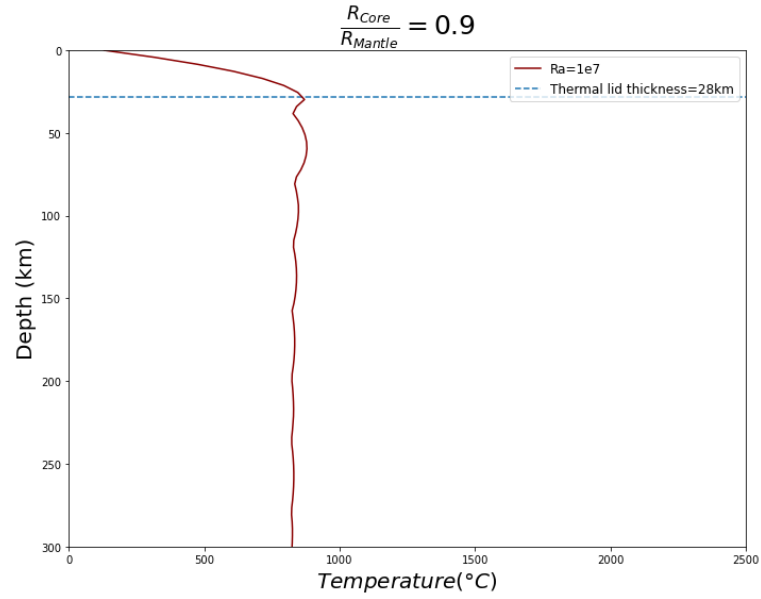


Figure A.19: Adiabatic profile for the first 300km in a CMB configuration 0.9R and $Ra=1e7$, the thickness of the thermal lid is defined finding the second derivative of the adiabat.

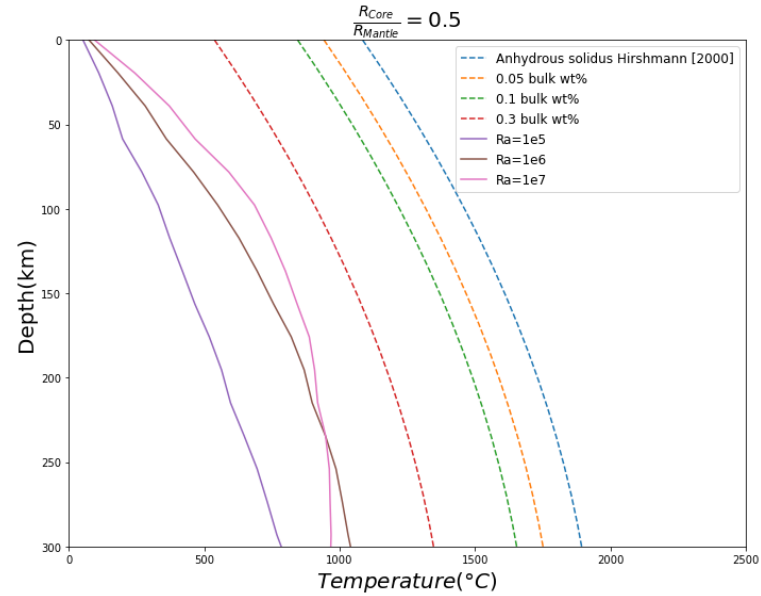


Figure A.20: Adiabatic profile for the first 300km in a CMB configuration 0.5R and different Ra with the parametrization for melting with volatiles. Profiles above the solidus temperature are melting, profiles below remain solid.

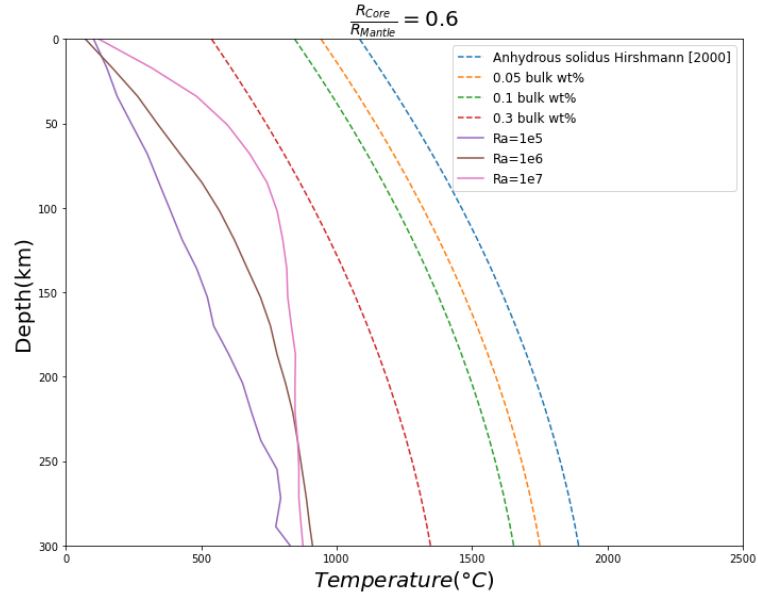


Figure A.21: Adiabatic profile for the first 300km in a CMB configuration 0.6R and different Ra with the parametrization for melting with volatiles. Profiles above the solidus temperature are melting, profiles below remain solid.

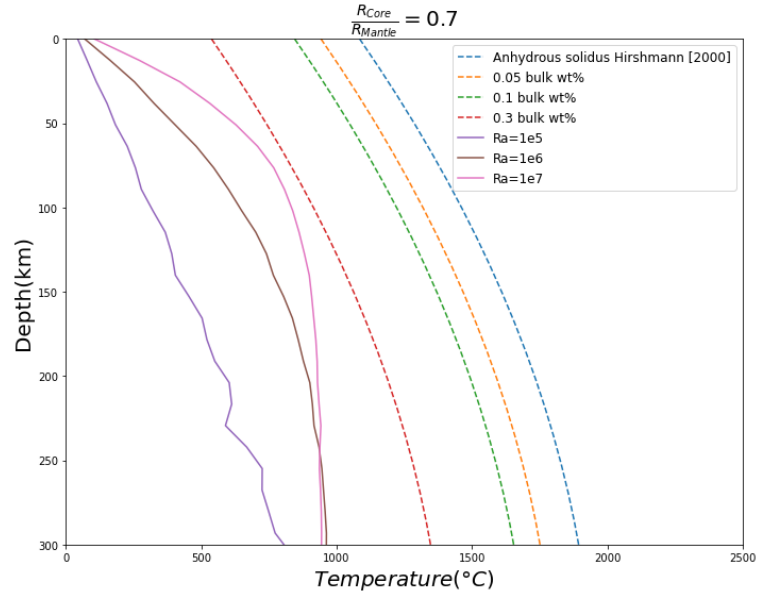


Figure A.22: Adiabatic profile for the first 300km in a CMB configuration 0.7R and different Ra with the parametrization for melting with volatiles. Profiles above the solidus temperature are melting, profiles below remain solid.

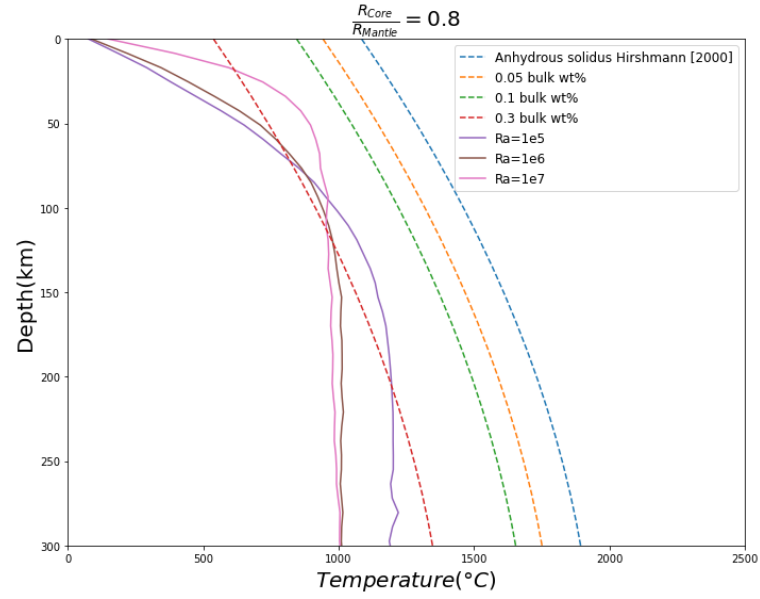


Figure A.23: Adiabatic profile for the first 300km in a CMB configuration 0.8R and different Ra with the parametrization for melting with volatiles. Profiles above the solidus temperature are melting, profiles below remain solid.

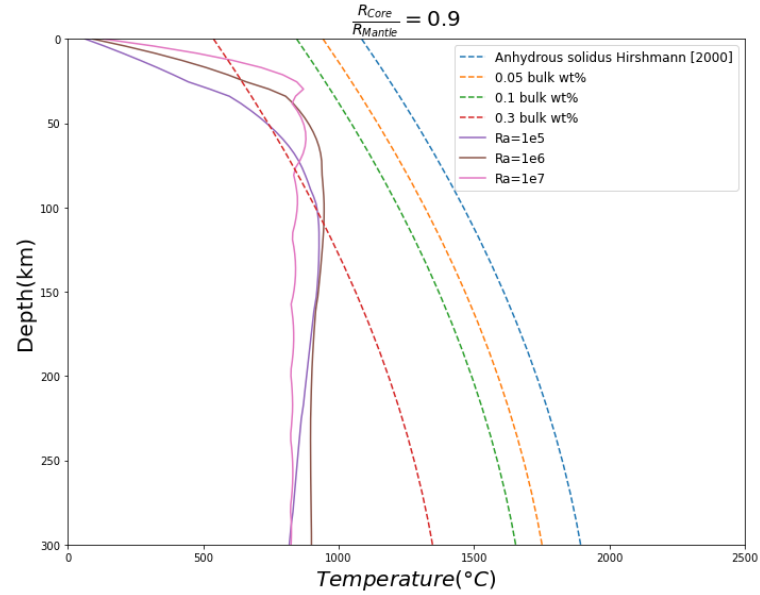


Figure A.24: Adiabatic profile for the first 300km in a CMB configuration 0.9R and different Ra with the parametrization for melting with volatiles. Profiles above the solidus temperature are melting, profiles below remain solid.

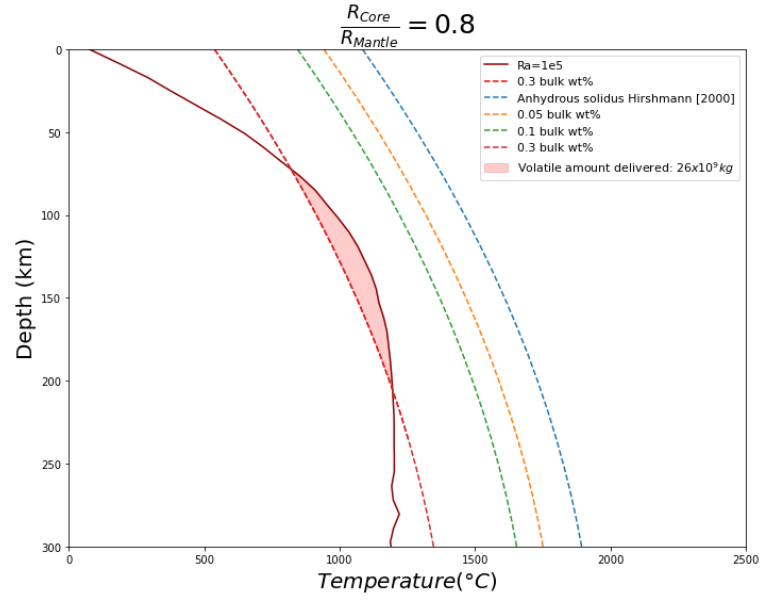


Figure A.25: Temperature profile of a planet with CMB configuration of $0.8R$ and $Ra=1e5$, showing presence of melt in the first 300km

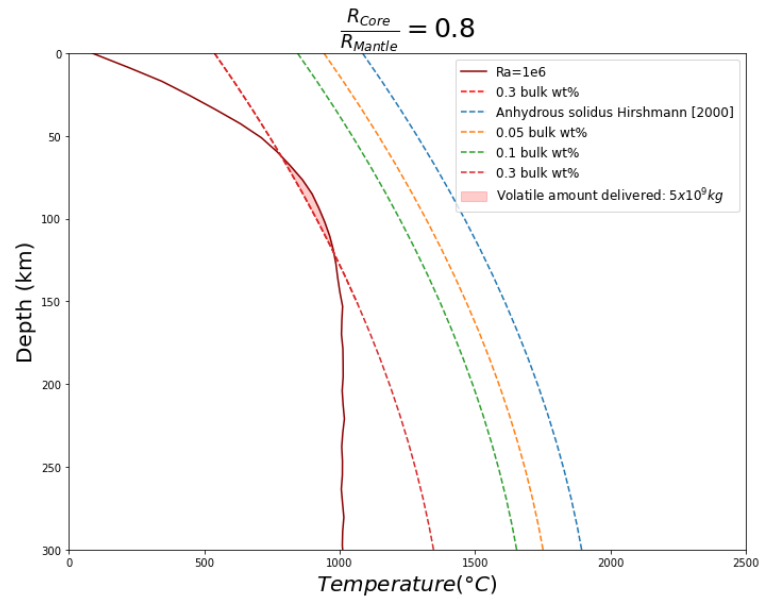


Figure A.26: Temperature profile of a planet with CMB configuration of $0.8R$ and $Ra=1e6$, showing presence of melt in the first 300km

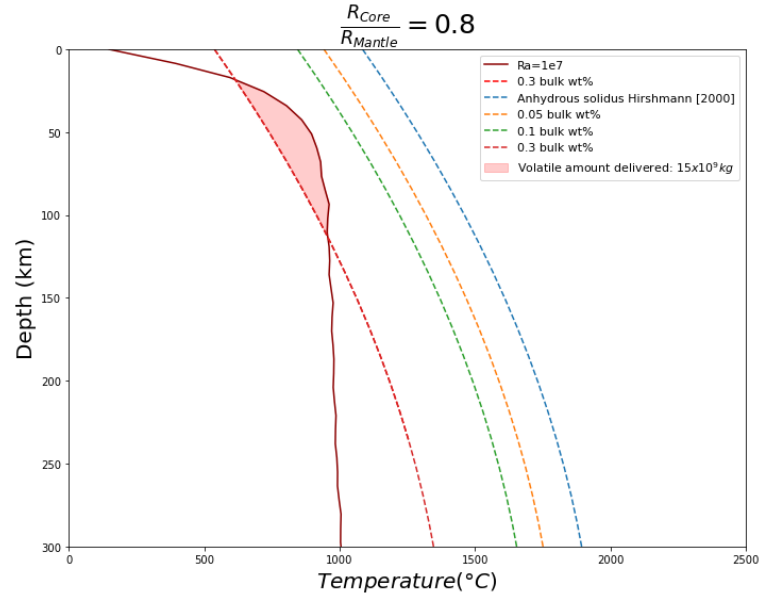


Figure A.27: Temperature profile of a planet with CMB configuration of $0.8R$ and $Ra=1e7$, showing presence of melt in the first 300km

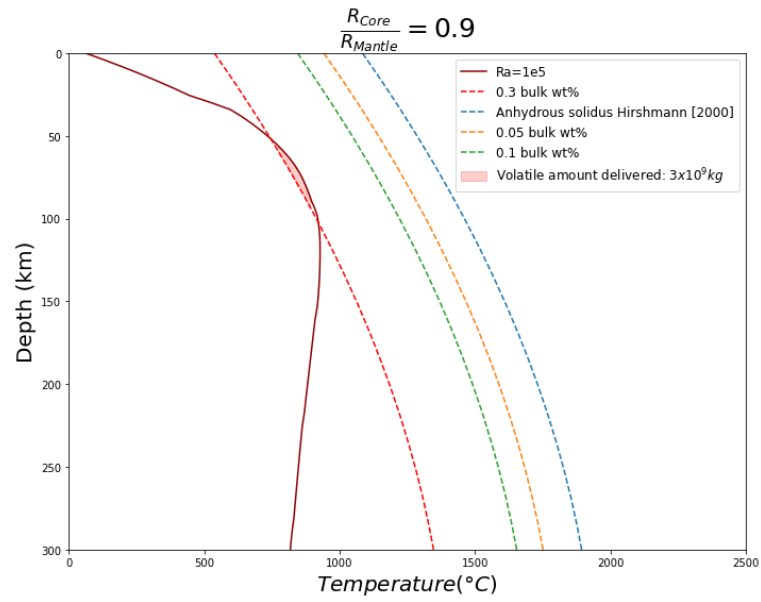


Figure A.28: Temperature profile of a planet with CMB configuration of $0.9R$ and $Ra=1e5$, showing presence of melt in the first 300km

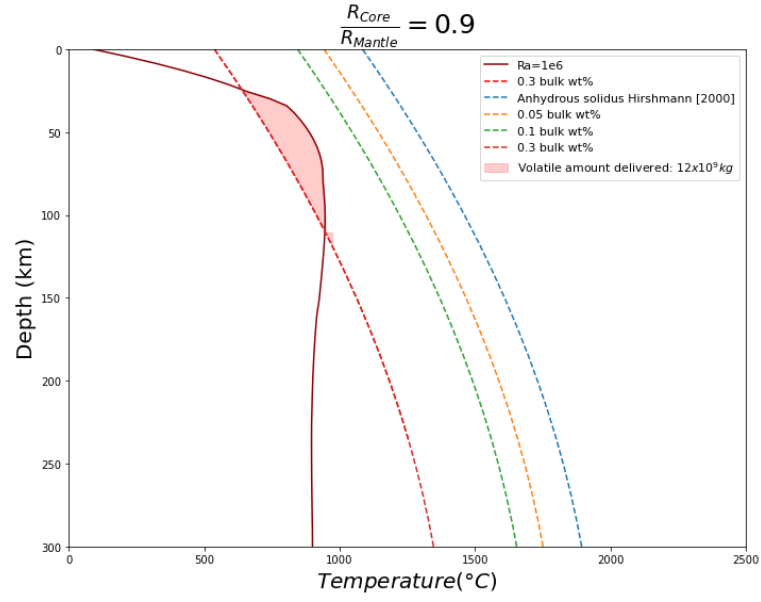


Figure A.29: Temperature profile of a planet with CMB configuration of $0.9R$ and $Ra=1e6$, showing presence of melt in the first 300km

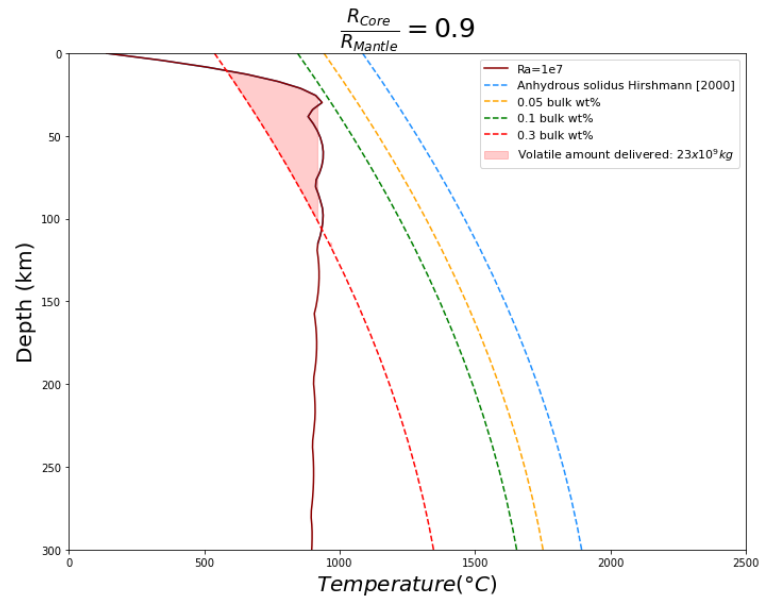


Figure A.30: Temperature profile of a planet with CMB configuration of $0.9R$ and $Ra=1e7$, showing presence of melt in the first 300km